Title

Improved dust representation in the Community Atmosphere Model

Journal

Journal of Advances in Modeling Earth Systems, 6(3)

ISSN

1942-2466

Authors

Albani, S

Mahowald, NM

Perry, AT

et al.

Publication Date

2014-09-01

DOI

10.1002/2013ms000279

AGU PUBLICATIONS

Journal of Advances in Modeling Earth Systems

RESEARCH ARTICLE
10.1002/2013MS000279

Improved dust representation in the Community Atmosphere Model

S. Albani[1,2], N. M. Mahowald[1], A. T. Perry[1], R. A. Scanza[1], C. S. Zender[3], N. G. Heavens[4], V. Maggi[2], J. F. Kok[1,5], and B. L. Otto-Bliesner[6]

[1]Department of Earth and Atmospheric Sciences, Cornell University, Ithaca, New York, USA, [2]Department of Environmental Sciences, University of Milano-Bicocca, Milano, Italy, [3]Department of Earth System Science, University of California, Irvine, California, USA, [4]Department of Atmospheric and Planetary Sciences, Hampton University, Hampton, Virginia, USA, [5]Now at Department of Atmospheric and Oceanic Sciences, University of California, Los Angeles, California, USA, [6]National Center for Atmospheric Research, Boulder, Colorado, USA

Key Points:
- Refined physical parameterizations of dust in the Community Atmosphere Model
- Improved soil erodibility, size distributions, wet deposition, and optics
- Better representation of dust cycle, size distributions, and radiative forcing

Supporting Information:
- Figure S1
- README
- Text1
- Table S1

Correspondence to:
S. Albani,
s.albani@cornell.edu

Citation:
Albani, S., N. M. Mahowald, A. T. Perry, R. A. Scanza, C. S. Zender, N. G. Heavens, V. Maggi, J. F. Kok, and B. L. Otto-Bliesner (2014), Improved dust representation in the Community Atmosphere Model, *J. Adv. Model. Earth Syst.*, *6*, 541–570, doi:10.1002/2013MS000279.

Received 24 OCT 2013
Accepted 12 MAY 2014
Accepted article online 14 MAY 2014
Published online 16 JUL 2014

Abstract Aerosol-climate interactions constitute one of the major sources of uncertainty in assessing changes in aerosol forcing in the anthropocene as well as understanding glacial-interglacial cycles. Here we focus on improving the representation of mineral dust in the Community Atmosphere Model and assessing the impacts of the improvements in terms of direct effects on the radiative balance of the atmosphere. We simulated the dust cycle using different parameterization sets for dust emission, size distribution, and optical properties. Comparing the results of these simulations with observations of concentration, deposition, and aerosol optical depth allows us to refine the representation of the dust cycle and its climate impacts. We propose a tuning method for dust parameterizations to allow the dust module to work across the wide variety of parameter settings which can be used within the Community Atmosphere Model. Our results include a better representation of the dust cycle, most notably for the improved size distribution. The estimated net top of atmosphere direct dust radiative forcing is -0.23 ± 0.14 W/m^2 for present day and -0.32 ± 0.20 W/m^2 at the Last Glacial Maximum. From our study and sensitivity tests, we also derive some general relevant findings, supporting the concept that the magnitude of the modeled dust cycle is sensitive to the observational data sets and size distribution chosen to constrain the model as well as the meteorological forcing data, even within the same modeling framework, and that the direct radiative forcing of dust is strongly sensitive to the optical properties and size distribution used.

1. Introduction

Mineral dust is entrained into the atmosphere by the action of wind stress on the land surface. Most sources of dust aerosols are arid or semiarid areas with low vegetation cover and easily erodible soils or fine-grained loose surface deposits [*Gillette et al.*, 1998; *Prospero et al.*, 2002]. With typical atmospheric lifetimes of a few days [*Alfaro and Gomes*, 2001; *Forster et al.*, 2007; *Han and Zender*, 2010], dust aerosols can travel long distances [*Prospero and Nees*, 1986] and interact with the climate system, both directly by absorbing and scattering short (SW) and long-wave (LW) radiation and indirectly through interactions with other aerosols and clouds [*Miller and Tegen*, 1998; *Forster et al.*, 2007; *Perlwitz and Miller*, 2010]. In addition, dust deposition to the surface can alter surface albedo [*Conway et al.*, 1996] and impact biogeochemical cycles [*Martin et al.*, 1990; *Mahowald*, 2011]. Sedimentary records from ice cores [e.g., *Petit et al.*, 1999], marine cores [e.g., *Rea*, 1994], and terrestrial deposits [e.g., *Pye*, 1995] show that dust deposition varied greatly over a broad range of time scales, most remarkably on the glacial-interglacial time scales [e.g., *Lambert et al.*, 2008; *Albani et al.*, 2012a], but also within interglacials [*deMenocal et al.*, 2000] and in recent centuries/decades [*McConnell et al.*, 2007; *Mulitza et al.*, 2010].

The role of mineral aerosols in the climate system has motivated their inclusion in climate models [e.g., *Tegen and Fung*, 1994; *Schulz et al.*, 1998; *Mahowald et al.*, 1999; *Ginoux et al.*, 2001] and the monitoring of characteristics of the present-day dust cycle, through long-term in situ [e.g., *Prospero and Lamb*, 2003] or remote sensing observations [e.g., *Holben et al.*, 1998; *Kaufman et al.*, 2001] and by intensive field campaigns [e.g., *Heintzenberg*, 2009]. In addition, extensive compilations of past dust deposition rates from paleoarchives [*Kohfeld and Harrison*, 2001] served to test climate simulations [*Tegen et al.*, 2002], especially for the glacial-interglacial comparison [*Mahowald et al.*, 2006b; *Albani et al.*, 2012b].

Aerosol interactions with climate still constitute one of the major uncertainties in assessing the global average radiative forcing (RF) [*Forster et al*., 2007], and uncertainties in modeling the dust cycle can be still quite large [*Huneeus et al*., 2011]. Beside the difficulties in realistically simulating dust emissions and consequently the magnitude of the dust cycle [e.g., *Cakmur et al*., 2006], major sources of uncertainty include the size distribution and optical properties of dust [*Tegen*, 2003]. Despite the early recognition of the importance of dust size distributions in modeling [*Schulz et al*., 1998; *Tegen and Lacis*, 1996], the most recent reviews still place emphasis on the need of devoting more attention to this feature [*Huneeus et al*., 2011; *Formenti et al*., 2011; *Maher et al*., 2010]. This is a challenging task as shown by studies comparing different observational techniques [e.g., *Reid et al*., 2003; *Mahowald et al*., 2013].

Our dust model was previously incorporated into the Community Climate System Model in version 3 (CCSM3) [*Mahowald et al*., 2006b], and it was extensively used and tested for a variety of experiments [e.g., *Mahowald et al*., 2006c, 2011] and on different time scales [*Mahowald et al*., 2010; *Albani et al*., 2012b].

In this work, we used the Community Earth System Model Version 1 (CESM1). More specifically, we used two release versions of the model: (1) the Community Atmosphere Model version 4 (CAM4) [*Neale et al*., 2010b; *Gent et al*., 2011] in the framework of the Community Climate System Model version 4 (CCSM4), which is also part of CESM1, and (2) the Community Atmosphere Model version 5 (CAM5) [*Neale et al*., 2010a; *Liu et al*., 2012]. We performed a series of tests to optimize some key physics parameterizations related to dust (i.e., soil erodibility, dust emission size distributions, wet deposition, and optical properties). We show some relevant improvements compared to the release versions, in comparison with observations, especially in terms of magnitude of the dust cycle, size distributions, and optical properties. We propose a tuning method which allows the dust cycle to be tuned for the wide variety of model options available within the CESM (e.g., reanalysis winds versus fully coupled, different resolutions) [e.g., *Cakmur et al*., 2006; *Mahowald et al*., 2006b]. We also show a dust simulation for a CCSM4 case for the Last Glacial Maximum (LGM), corresponding to $\sim$21,000 years before present (21 ka BP). The effects of the improved dust parameterization on dust radiative forcing and the sensitivity to specific changes are then described and compared to observations (section 3).

2. Methods

2.1. Model Description

The CCSM4 is a general circulation climate model with atmosphere, land, ocean, and sea ice components linked by a flux coupler. The atmospheric component (CAM4) uses a finite volume dynamical core, rather than the CCSM3 spectral core [*Gent et al*., 2011]. The CCSM4 model is part of the Paleoclimate Modeling Intercomparison Project Phase 3 (PMIP3) [*Otto-Bliesner et al*., 2009] and the Coupled Model Intercomparison Project Phase 5 (CMIP5) [*Taylor et al*., 2012] experiments. The CESM1 also includes a new version of the atmospheric model (CAM5). With respect to CAM4, enhancements in physical parameterizations allow, in particular, the simulation of full aerosol cloud interactions including cloud droplet activation by aerosols, precipitation processes that account for cloud particles size-dependent behavior, and explicit radiative interactions, in turn making it possible to simulate the aerosol-cloud interactions [*Neale et al*., 2010a; *Liu et al*., 2012]. CAM5 also participated in the CMIP5 experiments. In this study, we consider the dust in both CAM4 and CAM5 versions of the model. Prognostic dust is available in CESM1, and the default dust model largely follows the same treatment from CCSM3 [*Mahowald et al*., 2006b; *Yoshioka et al*., 2007].

The dust model consists of three major components: (1) emission, (2) vertical transport, wet and dry deposition, and (3) radiative effects.

The dust emission scheme in CESM1 [*Oleson et al*., 2010] follows the CCSM3 implementation [*Mahowald et al*., 2006b] of the Dust Entrainment And Deposition (DEAD) model. The dust emission scheme is based on a saltation-sandblasting process dependent on modeled wind friction velocity, soil moisture, and vegetation/snow cover [*Zender et al*., 2003a]. This part of the dust model is embedded in the land model (CLM4) [*Lawrence et al*., 2011]. The saltation process is represented by a horizontal mass flux dependent on the excess wind friction velocity over a threshold [*White*, 1979]. Modeled wind friction velocity is corrected by considering the Owen effect, i.e., the increase in wind friction speed due to the positive feedback from saltation [*Gillette et al*., 1998]. The wind friction velocity threshold is calculated following *Iversen and White* [1982], and it is corrected for drag partition [*Marticorena and Bergametti*, 1995] and for the inhibition of

saltation due to soil moisture [*Fécan et al*., 1999]. The latter process is negligible in the current model setup, because of the particular choice of a tuning factor that, in fact, sets the moisture inhibition threshold close to zero [*Oleson et al*., 2010]. The parameterization assumes the availability of optimal size particles for saltation (75 μm) [*Iversen and White*, 1982]; thus, saltation occurs whenever the wind friction velocity threshold is exceeded in the model [*Marticorena and Bergametti*, 1995]. Dust emission by sandblasting is represented by a vertical mass flux, given by the product of the horizontal mass flux multiplied by the sandblasting mass efficiency, which depends on the clay content of the parent soil and is assumed to be size and drag-independent [*Marticorena and Bergametti*, 1995]. The model's prescribed mineral soil texture data set [*Bonan et al*., 2002] is based on the International Geosphere-Biosphere Programme (IGBP) soil data set (Global Soil Data Task 2000) of 4931 soil mapping units and their sand and clay content for each soil layer.

The vertical flux is corrected by considering just the erodible fraction of each model surface grid cell, i.e., the fractional area not covered by lakes, wetlands, or snow. In the same fashion, the vertical flux is also scaled by a factor inversely related to the frozen soil fraction and vegetation cover, whereas dust mobilization is completely suppressed above a certain vegetation cover threshold—we use a Leaf Area Index of 0.3, based on observations of dust emission [*Okin*, 2008]. Differences in soils' susceptibility to erosion (i.e., related to soil grain size and textures) are incorporated by multiplying the dust emissions by a geomorphic soil erodibility factor [*Zender et al*., 2003b]—based on the concept of preferential sources [*Ginoux et al*., 2001]. The soil erodibility factor is a spatially varying scale factor for dust emissions, based on the regional topography (it is proportional to the upstream runoff area) and accounts for the concept that topographic lows are hot spots for dust production [*Prospero et al*., 2002; *Zender et al*., 2003b] and is applied in the CAM. Alternative approaches in representing hot spots may result in different regional emphases on dust mobilization [*Cakmur et al*., 2006]. The vertical dust flux is assumed to be size-distributed in a globally uniform trimodal lognormal probability density function, defined as the "background" modes of dust (source modes) suggested by *d'Almeida* [1987].

CAM4 has a Bulk Aerosol Model (BAM) parameterization of the dust size distribution [*Neale et al*., 2010b], where emission fluxes have a fixed size distribution partitioning into four size bins (bin1 = 0.1–1.0 μm; bin2 = 1.0–2.5 μm; bin3 = 2.5–5.0 μm; bin4 = 5.0–10.0 μm in diameters) [*Mahowald et al*., 2006b]. The vertical dust mass flux is passed to CAM4 by considering the sum of the fractions of each of the source modes that falls in the size range of each of the transport bins of the BAM [*Schulz et al*., 1998; *Zender et al*., 2003a]. The BAM subbin size distribution is fixed based on a log-normal distribution with mass median diameter of 3.5 μm and standard deviation of 2.0 [*Zender et al*., 2003a].

Dust transport is controlled by the CAM4 tracer advection scheme [*Neale et al*., 2010b]. Modeled dry deposition for dust includes gravitational and turbulent deposition processes [*Zender et al*., 2003a]. Wet deposition of dust results from both convective and large scale rain and snow precipitation simulated in CAM4 and is dependent on prescribed solubility and prescribed scavenging coefficients [*Mahowald et al*., 2006b; *Neale et al*., 2010b]. Wet deposition include in-cloud and below-cloud precipitation. Solubility represents the fraction of dust that resides in the cloud water; it is size-independent and constant (0.15). In-cloud scavenging is performed assuming that the fraction of the aerosol residing in the cloud water is removed in proportion to the fraction of cloud water that is converted to rain through coalescence and accretion processes [*Neale et al*., 2010b]. The below-cloud scavenging [*Dana and Hales*, 1976; *Balkanski et al*., 1993] assumes that both rain and snow scavenge the aerosol below cloud by a first-order loss process, i.e., the product of the precipitation flux, the aerosol mass mixing ratio, and the collection efficiency (scavenging coefficient). The scavenging coefficient in the model is size-independent and constant (0.1) [*Neale et al*., 2010b].

Dust size distribution (i.e., the relative proportions of mass in each of the size bins) evolves in time in response to transport and deposition processes, first of all because of the size-dependent parameterization of dry and wet deposition. In addition, there is a more subtle interaction between the vertical profile of the dust and the vertical distribution of precipitation, since wet deposition removal only acts on dust below and within the cloud during an event [*Mahowald et al*., 2006b; *Albani et al*., 2012b]. Thus, if the vertical distribution has more dust mass lower in the atmosphere (below the cloud), due to either large scale or boundary layer mixing processes, this will change the evolution of dust size and mass (e.g., see more discussion in *Albani et al*. [2012b]).

For aerosol transport, deposition, and radiation interactions, CAM5 instead uses a Modal Aerosol Model (MAM3). Dust emission works the same way as described above for CAM4-BAM, whereas transport and

Table 1. Schematic of Default Versus New Set of Parameterizations

Physical Process	Release Parameterization	New Parameterization
Soil erodibility	*Mahowald et al.* [2006]	New tuning; this work
Emissions size distribution	(0.038, 0.11, 0.17, 0.67); *Mahowald et al.* [2006]	(0.011, 0.087, 0.277, 0.625); *Kok* [2011]
Wet deposition	Dust solubility = 0.15; scavenging coeff = (0.1,0.1,0.1,0.1)	Dust solubility = 0.3; scavenging coeff = (0.1,0.1,0.3,0.3)
Dust optics	CAM4/CAM5 default	This work

deposition—and the evolution of dust size distribution as a consequence—follow CAM5-MAM3 parameterizations. Dust in MAM3 is partitioned in two transport modes: accumulation (0.1–1.0 μm) and coarse (1.0–10.0 μm in diameters) [*Neale et al*., 2010a]. Both the number and mass mixing ratio of aerosols are predicted in each mode. In addition, the accumulation and coarse modes in the CAM5-MAM3 parameterization are internally mixed within each mode, meaning, for example, that all the mass in the accumulation mode particles are assumed to be well mixed [*Liu et al*., 2012], and thus sulfate is homogeneously mixed with dust when present in the same mode. Only sea salt and dust can be found in the coarse mode and are subject to gravitational settling, similar to CAM4, but based on the different size representation in CAM5 [*Liu et al*., 2012]. This reduction in the resolution of the size distribution in the CAM5 model compared to CAM4 does make it more difficult to evaluate the evolution of the dust size, and thus here we only evaluate the dust size distribution downwind using the CAM4.

Dust aerosols in the model scatter and absorb solar and terrestrial radiation, altering the atmospheric radiation balance. For the short-wave (SW) radiation-dust interactions, the release version of the CAM4 and CAM5 model uses the OPAC optical parameters [*Hess et al*., 1998], and the dust optical properties are derived from Mie calculations for the size distribution represented by each size bin [*Neale et al*., 2010b]. Note that the OPAC optical parameters are outdated [e.g., *Sinyuk et al*., 2003] and were accidentally included. We test the impact of these changes in optical properties with more recent estimates of the dust refractive indices, similar to what was already in use for CAM3 [*Yoshioka et al*., 2007]. Long-wave (LW) interactions are based on *Volz* [1973] refractive indices. Dust is assumed to be externally mixed with other aerosol species in the CAM4 model for radiation calculations. In CAM5-MAM3, however, dust and sea salt aerosols are internally mixed in the coarse mode, and dust is considered to be internally mixed with all aerosols in the accumulation mode. In addition in CAM5-MAM3 dust particles are hygroscopic and can undergo water uptake based on the equilibrium Kohler theory. In this case, their optical properties are calculated according to *Ghan and Zaveri* [2007]. The models also include snow albedo changes in response to dust (and black carbon) deposition, although snow albedo changes are dominated by black carbon deposition [*Flanner et al*., 2007; *Oleson et al*., 2010].

2.2. Observational Data Sets and Diagnostics

Evaluating the model's ability to reproduce different features of the dust cycle requires an adequate set of observations and a protocol that makes comparisons consistent [*Cakmur et al*., 2006; *Huneeus et al*., 2011]. The goal of the comparison is not to obtain an exact match with a specific datum, but rather to enhance the ability to reproduce the overall features, given the characteristics, uncertainties, and errors in both models and observations [e.g., *Cakmur et al*., 2006; *Albani et al*., 2012b]. In this work, we focused on columnar (Aerosol Optical Depth (AOD) or column load) and surface (atmospheric concentration and deposition flux) properties of the global dust cycle, by considering their magnitude, spatial distribution, size distribution, seasonality, and relation with the dust sources (Table 2, supporting information Text S1;, and Table S1). With "magnitude" of dust cycle, we refer to the global amount of dust, either in terms of emissions/deposition, dust burden, or globally averaged AOD.

Observational constraints for columnar dust properties are based on the AERONET network [*Holben et al*., 1998]. We considered the AOD Version 2 Direct Sun Algorithm, Level 2.0 (data are prefield and postfield calibrated, automatically cloud cleared, and manually inspected) data and selected a subset of stations based on filtering criteria in terms of data quality and by restricting to dust-dominated AOD sites. We considered a minimum number of days of measurements per month (10 days), full climatological annual cycle over the observational period, and average annual Angstrom Exponent <1.2 (the lower the Angstrom Exponent, the larger the dust fraction) [*Dubovik et al*., 2002] (Text S1). For the AERONET size distributions, we considered

Table 2. Observational Datas Sets Used in This Work and Related Dust Properties for Comparison With the Two Models

Property	Feature	Data Set	Reference	Metric	Code	CAM4-BAM	CAM5-MAM
AOD	Magnitude	AERONET	*Holben et al.* [1998]	AOD, annual average	O1	x	x
AOD	Seasonality	AERONET	*Holben et al.* [1998]	AOD, monthly average	O2	x	x
Column load	Size distribution	AERONET	*Dubovik and King* [2000]	Correlation for 1–10 μm range	O3	x	
Surface conc.	Magnitude	U. Miami	*Prospero et al.* [1998]	Concentration ($\mu g/m^3$), annual average	O4	x	x
Surface conc.	Seasonality	U. Miami	*Prospero et al.* [1998]	Concentration ($\mu g/m^3$), monthly average	O5	x	x
Deposition	Magnitude	This work	This work (Text S1)	Modern flux (mg/m^2 yr)	O6	x	x
Deposition	Magnitude	This work	This work (Text S1)	LGM flux (mg/m^2 yr)	O7	x	
Deposition	Magnitude	This work	This work (Text S1)	Interglacial flux (mg/m^2 yr)	O8	x	
Deposition	Size distribution	This work	This work (Text S1)	Correlation for 1–10 μm range	O9	x	
Deposition	Provenance	This work	This work (Text S1 and Table S1)	Source apportionment	O10	x	x

Level 2.0 Almucantar Retrievals Version 2 [*Dubovik and King*, 2000] monthly data for the same stations, but applied a more restrictive filter on the Angstrom Exponent ($<$0.8), because in this case we will be comparing directly to simulated dust (rather than all aerosols) size distributions. The size data are reported as volume distributions distributed in 22 size bins dV(r)/dlnr and refer to the column integrated size distributions. We interpolate the AERONET retrievals size bins to the CAM4-BAM bins (Text S1) to allow a direct comparison.

Surface concentration measurements from high-volume filter collectors, shown as monthly averages, were taken from the University of Miami Ocean Aerosols Network [e.g., *Prospero and Nees*, 1986; *Prospero et al.*, 1989]. In addition, annual averages from compiled data sets for station data were also used [*Mahowald et al.*, 2009], although sites in industrialized areas were not included in the optimization described later.

Dust deposition flux data tables were compiled, based on merging and revising preexisting data sets (Text S1; Tables S2 and S3), for modern climate [*Ginoux et al.*, 2001; *Tegen et al.*, 2002; *Mahowald et al.*, 2009; *Lawrence and Neff*, 2009], the LGM [*Kohfeld and Harrison*, 2001; *Maher et al.*, 2010], and interglacial climate [*Kohfeld and Harrison*, 2001; *Maher et al.*, 2010]. In particular, we restricted the size range of the observed dust flux to be consistent with the model (Text S1 and Table S2).

In addition, size distributions from midlatitudes [*Wu et al.*, 2009] and polar ice cores [*Steffensen*, 1997; *Delmonte et al.*, 2004; *McConnell et al.*, 2007] were reported at the model's size bins for comparison.

We also reviewed available information of dust provenance, for both present/interglacial and LGM climates (Text S1 and Table S1), in order to help refine the soil erodibility maps to represent more realistically the relative intensity of different source areas. The use of the geomorphic soil erodibility factor alone is not able to fully constrain the regional variability in the magnitude of dust emissions, at least as recorded in remote dust "sinks," although it is possible that still inadequate simulation of the wind patterns and/or removal processes may have a role. Spatially denser observational data sets would help the scientific community to better disentangle these issues.

In addition we considered the CALIOP (Cloud-Aerosol Lidar with Orthogonal Polarization) layer product to evaluate the vertical profiles of the model aerosol extinction [*Koffi et al.*, 2012].

2.3. Model Improvements

In this work we introduce a set of modifications to improve the release versions of the dust model in CAM, involving (a) dust emission size distributions, (b) wet deposition, (c) optical properties, and (d) soil erodibility (Table 1). The model improvements were performed as a three-step process: (1) we conducted a set of preliminary simulations to test changes to (a) dust emission size distributions and (b) wet deposition; (2) we adopted the proposed changes in (a) and (b), included changes in the dust optical properties (c), and conducted a set of simulations where dust was only emitted from one macroarea at a time, each broadly corresponding to a continent or subcontinent; (3) we spatially optimized the soil erodibility maps by producing scale factors specific to each of the macroareas. The full set of changes was then applied to the model and long-term simulations were conducted for a few different model configurations, together with corresponding control cases using the release version of the model. In addition, a simulation of the LGM climate with the refined parameterization set, and a few short sensitivity studies were conducted. The specific changes are detailed below, while the different simulation setups are described in the next section.

Here we describe the changes in the model compared against the release CAM4, which was based on the *Mahowald et al*. [2006b] study, except for the optical parameters, as discussed below. First, the distribution of dust in the four bins (or in the accumulation/coarse in the CAM5) was changed according to the brittle fragmentation theory for dust emissions [*Kok*, 2011]. That theory assumes that dust emissions are produced largely by the fragmentation of soil dust aggregates by the impacts of saltating particles, in the same way that brittle materials shatter upon sufficiently energetic impacts. Major implications are that (a) emitted dust size distribution is independent from wind speed, or better, from wind friction velocity and (b) that the dependence of dust size distribution on soil properties is of secondary importance. In the implementation of the theory for this study, we assume no dependence of dust size on soil properties. As such, dust size distribution is fixed for the emissions in the model, and it was derived by fitting the distribution derived in *Kok* [2011] to the model bins (CAM4-BAM) or modes (CAM5-MAM3) (Table 1).

In addition, in order to better match the observations, especially dust concentration and AOD at remote locations (see section 3.1), the wet deposition in CAM4 was changed by increasing the solubility for all dust particles from 0.15 to 0.30, similar to that in CAM5 [*Liu et al*., 2012; *Ghan et al*., 2012], and using a larger below-cloud scavenging coefficient for large particles (Table 1) [e.g., *Andronache*, 2003].

For the release versions of CAM4 and CAM5, SW optics from *Hess et al*. [1998] were accidentally included, instead of the more accurate values from CCSM3 [*Yoshioka et al*., 2007; *Mahowald et al*., 2010] for both the CAM4 and CAM5 optics. The release version optics are largely based on *d'Almeida et al*. [1991]. Old measurements of the dust refractive index [e.g., *d'Almeida et al*., 1991; *Patterson et al*., 1977] yield optical properties that give dust the tendency to be too absorbing compared to observations [*Kaufman et al*., 2001; *Colarco et al*., 2002; *Sinyuk et al*., 2003; *Yoshioka et al*., 2007; *Balkanski et al*., 2007]. In addition, LW interactions, based on *Volz* [1973] refractive indices, were turned off in the CAM4 default version, although they were included in the CAM5 release. For the optical properties used in this study, we represent dust as an internal mixture of minerals, with globally uniform, size-independent mineral fractions, which simplifies the regional and size-dependent aspects of this complex multicomponent aerosol. We include the primary mineral classes of dust (quartz, aluminosilicates, clays, carbonates, and iron-bearing minerals) represented by specific minerals mixed in proportions that are consistent with the ranges reported in atmospheric dust and its parent soils [*Pye*, 1987; *Claquin et al*., 1999] and that also yield agreement with bulk optical properties observed in dusty regions. The specific mineral composition is, by volume, 47.6% quartz, 25% illite, 25% montmorillonite, 2% calcite, and 0.4% hematite. The assumed densities are 2660 kg/m^3 for quartz, 2750 kg/m^3 for illite, 2350 kg/m^3 for montmorillonite, 2710 kg/m^3 for calcite, and 5260 kg/m^3 for hematite. Radiative forcing is sensitive to mineralogical and optical assumptions [*Sokolik et al*., 1998; *Sokolik and Toon*, 1999]. Solar radiation is particularly suited to absorption by iron-bearing minerals such as hematite and goethite [*Lafon et al*., 2006]. The optical properties of these minerals are combined into an effective medium using the Maxwell Garnett approximation [e.g., *Videen and Chylek*, 1998]. The resultant effective bulk optical properties are consistent with those inferred from observations of North African and Arabian dust (Figure 1).

To account for unrepresented source differences, soil erodibility maps were optimized for each model configuration [e.g., *Mahowald et al*., 2006b; *Albani et al*., 2012b; *Cakmur et al*., 2006]. The world is divided in different macroareas, broadly corresponding to continents or subcontinents. For each macroarea, we define a scale factor, and then we apply the full set of scale factors to the global soil erodibility maps. The soil erodibility map for current climate was first objectively optimized (similar to *Mahowald et al*. [2006b]) but then modified to account for dust provenance information (Table S1 and Figure S1). For the optimization (as in *Mahowald et al*. [2006b]), the logarithm in errors in AOD, concentration, and deposition are all squared and weighted equally, except that ice cores are weighted 10x, as believed to be more accurate (cores from mountainous areas, unlike those from polar ice sheets, may be a poor constraint for global models though, because of unresolved topography). We use the logarithm of the values, since we want to capture variability in deposition and concentration that varies over 4 orders of magnitude. Without using a logarithm, the optimization would be heavily weighted toward measurements with the highest values: there is a trade-off implied in balancing the weights of different observations, and we chose to give more emphasis on the long-range transport rather than the emissions. Because of errors in both modeling and observations, we only expect to match the data to about a factor of 10, especially for deposition [e.g., *Mahowald et al*., 2011].

The scale factors for the LGM soil erodibility maps (Figure S2), including explicitly glaciogenic sources [*Mahowald et al*., 2006b], were based on three criteria: matching (1) the observed LGM deposition and (2)

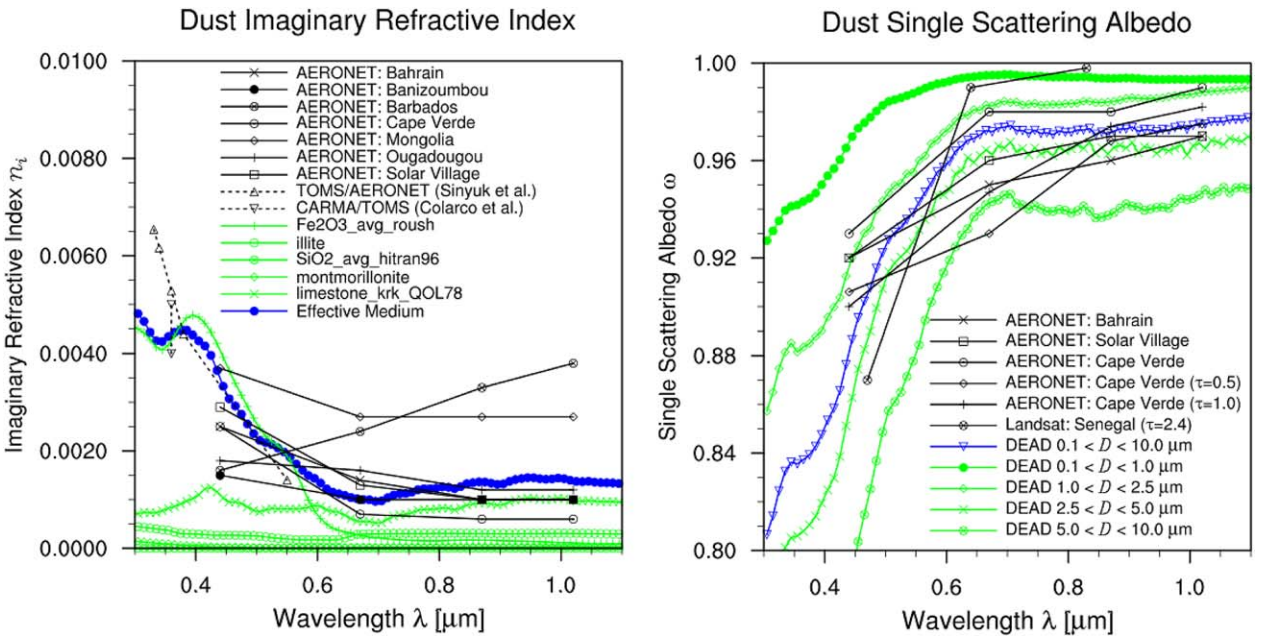

Figure 1. Wavelength dependence of dust optical properties in the visible part of the spectrum. (left) Imaginary refractive index of bulk dust and individual mineral components in our new model, compared with remote sensing observations. (right) Single scattering Albedo for bulk dust and individual size bins in our model (based on annual average simulation at Solar Village), compared to AERONET observations.

the LGM/interglacial deposition ratio (data set largely based on DIRTMAP3 [*Maher et al*., 2010], see Text S1 and Figure S2), as well as (3) considering the information on dust provenance in the LGM (Table S1 and Figure S3). Using LGM/interglacial observation and model deposition ratios requires knowledge of the preindustrial dust flux, about which we have less information than for either current or LGM [e.g., *Mahowald et al*., 2011]. In order to test that we simulate meaningful glacial/interglacial ratios, we considered as a rough approximation for interglacial dust deposition as half of that of current climate [*Mulitza et al*., 2010; *McConnell et al*., 2007; *Mahowald et al*., 2010, and references therein]. Lacking an explicit simulation of the preindustrial climate and assuming a globally uniform scale factor for dust emissions will produce some uncertainty, but this is probably comparable to considering preindustrial climate (and dust) as an estimate of average Holocene conditions, which is the time scale of the existing compilations of paleodust depositional estimates [e.g., *Maher et al*., 2010].

The evaluation of the tuning simulations (Table 3) was based on extensively comparing the simulated output with observations (Table 2). In Table 4, we summarize the performance of different cases. We show the model's ability to reproduce the overall magnitude of the dust cycle (median of the modeled/observed ratio at each site) and its variability range (Pearson's correlation of the model-observation pairs at each site), by analyzing dust AOD, surface concentration, and deposition. We also report the evaluation of the seasonal cycle for dust AOD and surface concentration (correlation). Finally, we report a metric (Pearson's correlation of modeled and observed size bin pairs) that allows comparing the modeled and observed shapes of dust size distributions for column load and deposition at selected sites for the supermicron size range.

2.4. Description of the Model Simulations

An overview of all the simulations considered in this study is reported in Table 3 (which includes a key to the cases nomenclature). We conducted a set of preliminary tests that use a computationally inexpensive setup (CAM4-BAM with slab ocean at $1.9^\circ \times 2.5^\circ$ latitude $\times$ longitude horizontal resolution) to test the effects of the new emissions size distribution (C4sr-k), and subsequently the refined wet deposition (C4sr-kw) compared to a base release case (C4sr).

The main cases presenting the comparison between observations and models that we used in this work are (1) a fully coupled simulation with CAM4-BAM ($0.9^\circ \times 1.25^\circ$, 26 vertical levels), run for 30 years (of which we considered the last 10 years) in equilibrium conditions for the year 2000 AD (C4fr and C4fn); (2) a standalone

Table 3. Description of the Model Simulations in This Work[a]

Case	Setup	Run Length, Spin-Up (Years)	Soil Erodibility	Emissions Size Distribution	Wet Deposition	Dust Optics
Preliminary Tests to Improvement Size and Wet Deposition						
C4sr	CAM4 slab ocean 2 × 2 current	2, 1	Release	Release	Release	Release
C4sr-k	CAM4 slab ocean 2 × 2 current	2, 1	Release	*Kok* [2011]	Release	Release
C4sr-kw	CAM4 slab ocean 2 × 2 current	2, 1	Release	*Kok* [2011]	This work	Release
Main Cases CAM4						
C4fr	CAM4 fully coupled 1 × 1 current	10, 20	Release	Release	Release	Release
C4fn	CAM4 fully coupled 1 × 1 current	10, 20	This work	*Kok* [2011]	This work	This work
C4wr	CAM4 2 × 2 MERRA winds	26, 1	Release	Release	Release	Release
C4wn	CAM4 2 × 2 MERRA winds	26, 1	This work	*Kok* [2011]	This work	This work
C4fn-lgm	CAM4 fully coupled 1 × 1 LGM	10, 40	This work	*Kok* [2011]	This work	This work
Main Cases CAM5						
C5wr	CAM5.3 2 × 2 MERRA winds	26, 1	Release	Release	Release	Release
C5wn	CAM5.3 2 × 2 MERRA winds	26, 1	This work	*Kok* [2011]	Release	This work
Sensitivity Tests for RF Calculation						
C4fn-rs	CAM4 fully coupled 1 × 1 current	2, 1	This work	Release	This work	This work
C4fn-ro	CAM4 fully coupled 1 × 1 current	2, 1	This work	*Kok* [2011]	This work	Release
C4fn-s2	CAM4 fully coupled 1 × 1 current	2, 1	This work	(0.02,0.09,0.27,0.62)	This work	This work
C4fn-lgm-s2	CAM4 fully coupled 1 × 1 LGM	2, 1	This work	(0.02,0.09,0.27,0.62)	This work	This work

[a]Key to cases nomenclature. C4/C5 identifies the model: CAM4-BAM or CAM5-MAM3. s/f/w identifies the coupling: standalone CAM with slab ocean model (s), fully coupled (f), or driven by reanalysis winds (w). r/n refers to the release (r) versus the new (n) parameterization. The field after the dash (-) identifies variations relative to the setup identified by the main field before the dash: Kok size (k); Kok size and new wet deposition (kw); last glacial maximum (lgm); release size (rs); release optics (ro); ×2 dust in bin1 emissions (s2).

case using CAM4-BAM (1.9° × 2.5°, 56 vertical levels) driven by MERRA reanalysis winds for the years 1980–2005 AD (1979 used as a spin-up period) (C4wr and C4wn); (3) a standalone case using CAM5-MAM3 (1.9° × 2.5°, 56 vertical levels) driven by MERRA reanalysis winds for the years 1980–2005 AD (1979 spin-up) (C5wr and C5wn). For all of the three component setups, two simulations were conducted, one using the release version of the model, and one with the refined parameterization.

The monthly mean seasonal cycle of vegetation cover is prescribed in terms of plant functional types (PFTs). The data set is derived from a variety of satellite products incorporated into present day PFT distributions with matching leaf area index values [*Lawrence and Chase*, 2007]. The fully coupled model setup includes a prognostic treatment of the terrestrial carbon and nitrogen cycles, which influence the seasonal timing of new vegetation growth and litterfall. At each time step, the prognostic leaf carbon pool is translated to a canopy-scale projected leaf area index [*Oleson et al*., 2010].

Nondust aerosols and aerosol precursors (black and organic carbon, dimethyl sulfide, sulfur oxides) emissions are prescribed based on data sets prepared for the Intergovernmental Panel on Climate Change's 5th Assessment Report (IPCC AR5) [*Lamarque et al*., 2010] and Aerocom specifications for injection heights and size distributions of primary emitted particles and precursor gases [*Neale et al*., 2010a], while sea salt aerosols emission is prognostic [*Mahowald et al*., 2006a], and in CAM5 depends on water temperature and 10 m wind speed [*Neale et al*., 2010a; *Liu et al*., 2012].

Table 4. Model Performance Compared to Observations (Fraction <10 μm)[a]

	C4sr	C4sr-k	C4sr-kw	C4fr	C4fn	C4wr	C4wn	C5wr	C5wn
Deposition correlation (O6)	0.73	0.73	0.70	0.77	0.78	0.93	0.90	0.78	0.77
Deposition model/observation ratio median (O6)	1.75	1.72	1.39	1.24	1.42	1.11	0.85	1.83	1.03
Surface concentration correlation (O4)	0.86	0.86	0.84	0.84	0.81	0.74	0.71	0.78	0.75
Surface concentration model/observation ratio median (O4)	2.38	2.38	1.05	2.37	0.93	1.37	0.46	1.70	0.81
AOD correlation (O1)	0.68	0.68	0.67	0.70	0.70	0.90	0.89	0.90	0.47
AOD model/observation ratio median (O1)	0.93	0.93	0.78	0.88	0.84	0.68	0.61	2.14	0.90
AOD seasonal correlation (O2)	0.46	0.46	0.41	0.6	0.41	0.79	0.69	0.57	0.67
Surface concentration seasonal correlation (O5)	0.24	0.25	0.29	0.3	0.31	0.5	0.45	0.31	0.49
Column size distribution correlation (O3)	−0.23	0.86	0.82	0.03	0.84	0.24	0.89		
Deposition size distribution correlation (O9)	0.1	0.18	0.41	0.21	0.29	0.41	0.77		

[a]Coding in the leftmost column (e.g., O*n*) refer to specific observational data set described in Table 2. The *p* values for all the correlations are <0.001, with the only exception of C5wn-AOD ($r = 0.47$, $p = 0.014$).

We also simulated dust for LGM equilibrium conditions (C4fn-lgm) with the refined parameterization set, considering 10 years after a 40 years spin-up period. We used initial conditions from a fully coupled climate equilibrium run with CAM4 [*Brady et al*., 2013], which followed the PMIP3 prescriptions for climate forcings, such as LGM orbital parameters, greenhouse gases concentrations and ice sheets topography, and preindustrial prescribed vegetation [*Otto-Bliesner et al*., 2009], and used prescribed present-day dust, same as C4fr. For our LGM simulation, we use an annual cycle of prescribed preindustrial vegetation (annual average: Figure S4) on the LGM topography mask, and similar to current climate this fully coupled simulation uses the carbon-nitrogen cycle terrestrial model. For use of the dust model in the LGM simulation, we removed the online dependence of dust mobilization on preindustrial vegetation cover. Instead we simulated a vegetation cover for the LGM equilibrium climate with BIOME4 [*Kaplan et al*., 2003] and incorporated the effects of vegetation in the soil erodibility map, by applying a scale factor at each grid cell proportional to the fraction of the grid cell available for dust emission. Similar to the online version, this mask allows emissions only in areas of low vegetative cover.

Finally, we conducted a set of sensitivity studies for radiative forcing calculations based on our base case simulations (1). Two simulations are intended to isolate the effects of the new versus old size distribution (C4fn-rs) and the new versus old optical properties (C4fn-ro). In addition, two more simulations (C4fn-s2 and C4fn-lgm-s2) are used to evaluate the sensitivity of modeled dust radiative forcing to uncertainties in the amount of submicron particles, for the current and LGM climate conditions, respectively. For those simulations, we doubled the relative contribution of dust emissions in the model bin1.

3. Results

3.1. Current Climate Dust

Several versions of the model were evaluated in this study (Table 3), but for simplicity, we show only detailed results for the online fully coupled simulation (C4fn). The preliminary tests on the new dust size distribution (C4sr-k) and wet deposition scavenging (C4sr-wk) parameterizations alone show an improved fit to the observations far from the source areas for both the size distribution and the magnitude (Table 4, O4 and O9 in particular, and Figure S5). This suggests that new theories on size distribution better match available observations [e.g., *Kok*, 2011; *Tanré et al*., 2001; *Cakmur et al*., 2006], as a consequence of switching mass at the emissions from both the clays and coarse silts into the fine silts range (2.5–5 μm: bin3) compared to the release size distribution (Table 1). In addition, the new wet scavenging parameterization improves the model's ability to simulate the observed spatial gradients of dust.

The release model's ability to reproduce the magnitude of the dust cycle, both annual mean and seasonal cycle, is quite variable. In general, using reanalysis winds results in a better reproduction of the annual cycle in CAM4 (Figures 7 and 8 and Table 4, O2 and O5). The modifications included here generally improve the ability of the model to simulate the dust cycle, although some degradation at specific sites or for specific variables is also seen (Figures 6–8 and Table 4).

3.1.1. Annual Averages

Comparisons of the annual mean deposition in the CAM4 (C4fn) to observations show that the model is able to simulate the spatial variability of annual mean deposition across 6 orders of magnitude (Figure 2). Deposition is greatly overestimated at two sites (Colle del Lys and Colle Gnifetti), probably because of unresolved orographic control on dust deposition on the Alps with the current model spatial resolution. Underestimation of deposition in the Argentinean Pampa is surprising, because the model matches well with offshore observations in the same region (James Ross Island) and is possibly related to large uncertainties in the estimates from terrestrial sediments or to a slightly inaccurate positioning of the dust sources for each of those sites.

The surface concentration of dust is reproduced in the model for almost all the sites considered within 1 order of magnitude (Figure 3).

Total (all aerosols) annual average AOD magnitude is reproduced by the model when compared to AERONET stations in dust-dominated areas, although the model tends to have less sharp spatial gradients than what would appear from the stations' observations (Figure 4). The spatially averaged modeled AOD over North Africa is close to the estimates from CALIOP and MODIS for the year 2007 [*Koffi et al*., 2012], with the

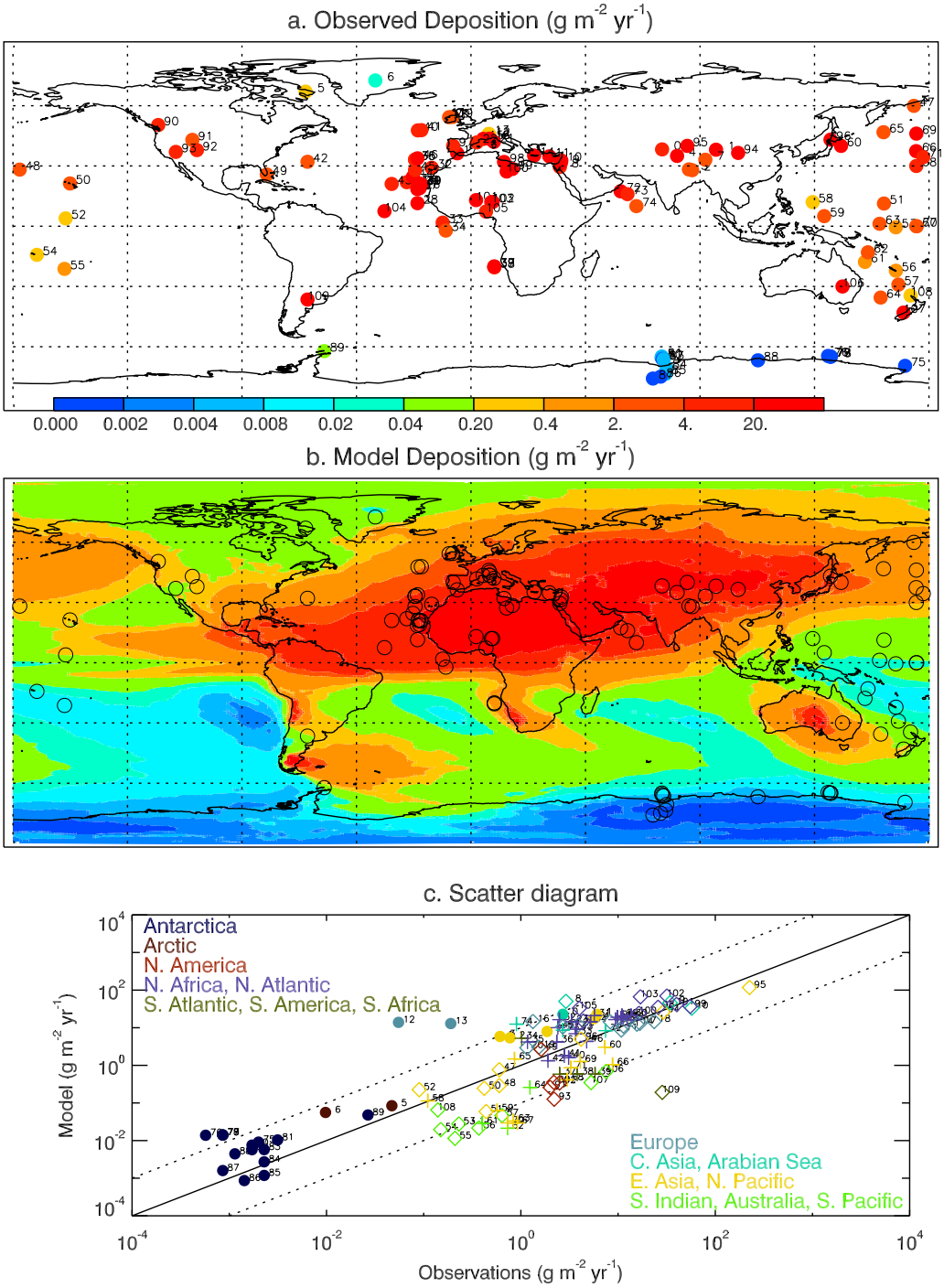

Figure 2. Comparison of simulated dust deposition (mg/m^2 yr) for the C4fn case, compared to observations of modern dust fluxes (Table 2). (top) Observations; (middle) model; (bottom) model versus observations scatterplot. Locations of observational sites are clustered in the scatterplots based on their geographical location. In the bottom, circles = ice cores; diamonds = terrestrial deposits; crosses = marine sediments.

exception of the CAM5 simulations that are substantially overestimating it (Figure 5). Vertical profiles of aerosol extinction will be discussed in detail later.

In summary, the effects on the magnitude of the dust cycle and its spatial variability (Figures 2–4) of the new parameterization set compared to the default one are shown in Figure 6, which considers both the cases with model (C4fr and C4fn) and reanalysis winds for CAM4 (C4wr and C4wn) and CAM5 (C5wr and

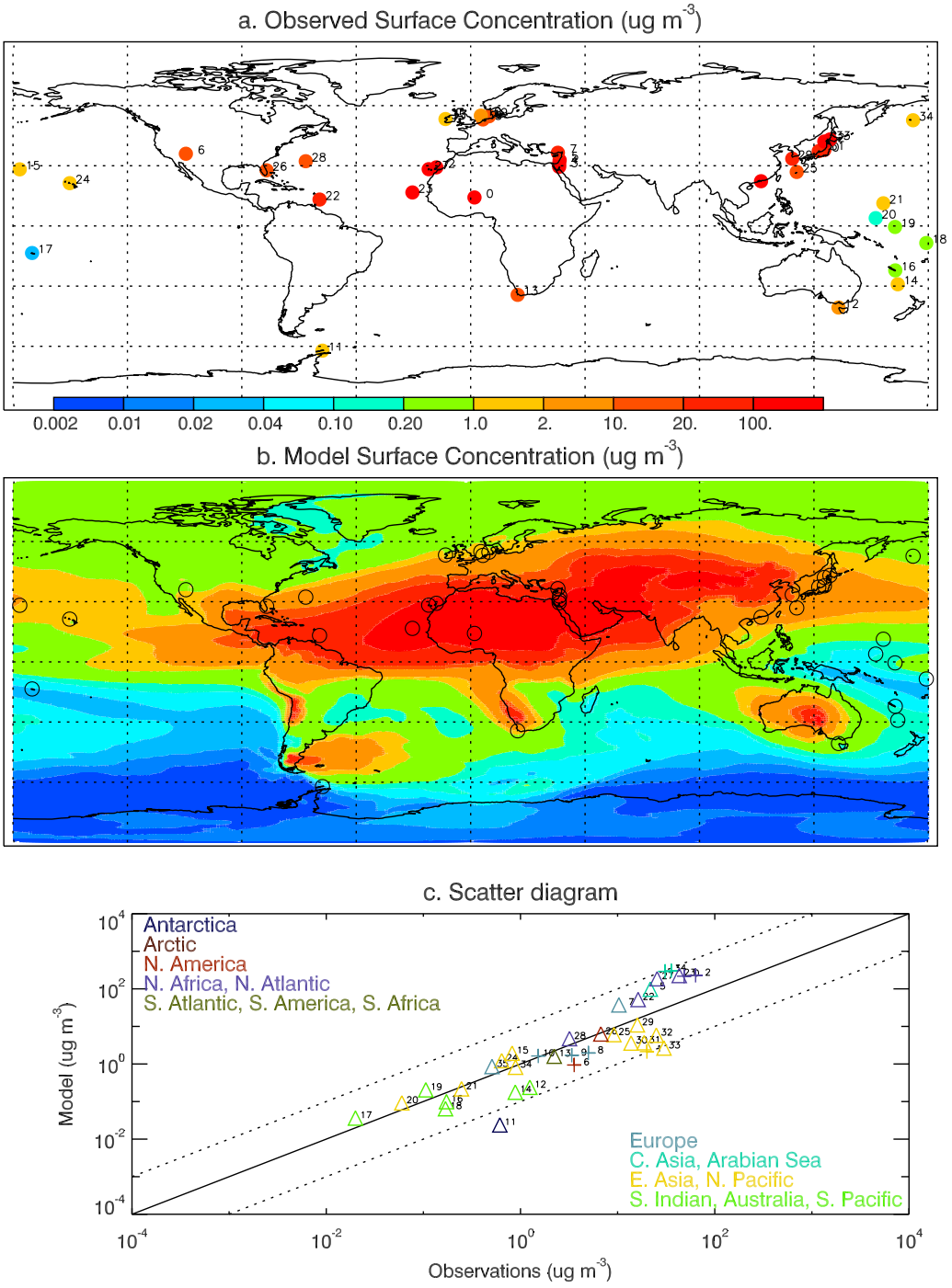

Figure 3. Same as Figure 2 for dust surface concentrations ($\mu g/m^3$). (bottom) Crosses = University of Miami sites (also reported in Figure 8); triangles = sites from *Mahowald et al.* [2009].

C5wn). While there is notable improvement over the default version for some variables, there is no parameterization that uniformly improves the fit to all three variables considered (AOD, dust surface concentration, and dust deposition). This is likely related to the large uncertainties that still exist in modeling dust emissions, as well as the model's meteorology [e.g., *Huneeus et al.*, 2011] and is consistent with previous general circulation model-based dust modeling [*Tegen and Fung*, 1994; *Mahowald et al.*, 2006a]. Notably, the cases using the refined parameterization set reduce the (high) bias compared to the observation, mainly, because of the new soil erodibility maps but also because of the refined wet deposition, the latter being more

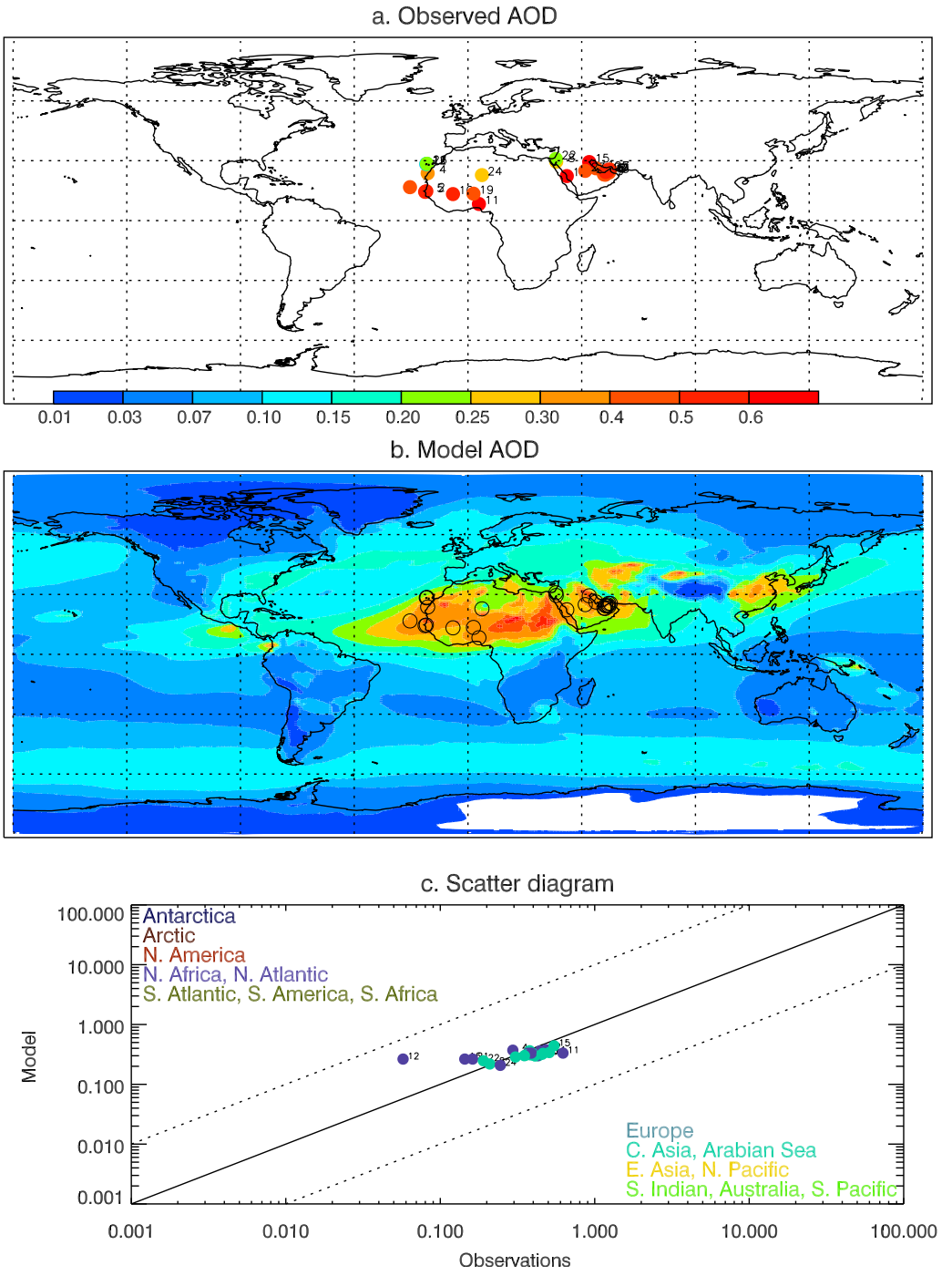

Figure 4. Same as Figure 2 for dust AOD.

relevant for remote locations (Table 4; C4sr-k versus C4sr-kw). Both the Aerocom models median and our model with the new parameterization tend to slightly underestimate AOD and dust surface concentration compared to the respective observational data sets, while deposition is simulated more similarly [*Huneeus et al.*, 2011], suggesting either issues in the consistency of these data sets or issues in modeling vertical mixing and/or deposition. Note that while the deposition and surface concentration data sets include information on spatial variability close to source regions as well as in remote regions, the AOD compilation is restricted to close to the main source areas, and thus is used only to constrain emissions.

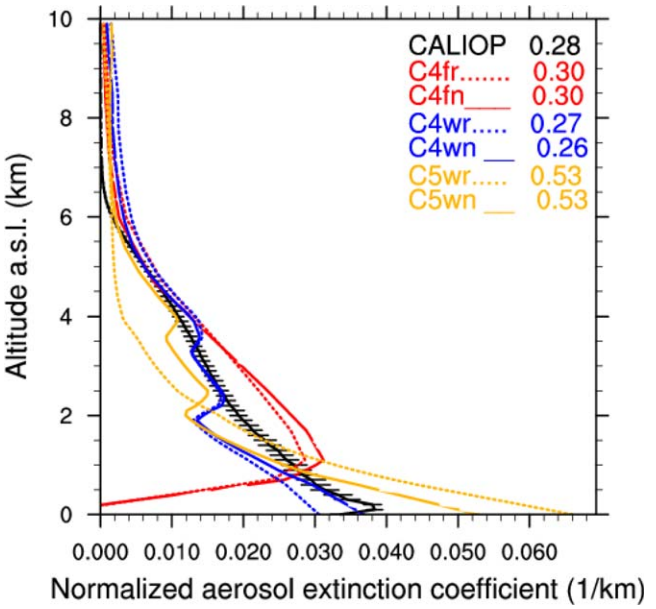

Figure 5. Model aerosol extinction profiles compared to CALIOP layer product data [*Koffi et al*., 2012]. Model extinction profiles (all aerosols) were averaged over the selected region, interpolated to the observations vertical levels, and normalized to unit AOD. CALIOP data are the 2007–2009 average (horizontal bars represent 1 standard deviation), model runs are 2000–2005 for the cases using reanalysis winds (C4wr, C4wn, C5wr, and C5wn) or 10 years for the fully coupled runs (C4fr and C4fn). See also Text S1.

In general using reanalysis (MERRA) winds implies differences in the model spatial resolution compared to the C4fn/C4fr cases, in addition to the offline meteorology versus the fully coupled setup. Because the target for model performance is the set of observational data sets we considered (Table 4), also transport and deposition come into play when determining the variables that are to be compared to the observations. In this respect, CAM5-MAM3 is quite different than CAM4-BAM in terms of subgrid scale physics as well as in the type of representation of the aerosols, i.e., binned/sectional versus modal. Because of the way we have tuned the model, as well as the changes in optical properties and sizes, there are very large differences between the default release version and the tuned versions (e.g., C5wr versus C5wn). Changes in the global tuning as shown here usually dominate the spatial distribution.

3.1.2. Seasonal Cycle

Next we consider the seasonal cycle of the modeled dust compared to observations. There is a tendency for the models to overpredict dust concentration at the peak season at many sites (Figures 7 and 8) (see also section 4.2). This feature was improved in the simulations with the new wet deposition parameterization and the refined soil erodibility maps. The refined soil erodibility maps may improve the seasonal cycle by adjusting the relative proportions of dust from different sources. A possible explanation for the remaining poor match with the seasonal cycle is that vertical mixing in the model may not be accurate (see section 4.2). Note that this is true whether the model is driven by online winds, or reanalysis winds, and does not change with the CAM5 versus CAM4, which have quite different subgrid scale physics (e.g., boundary layer, convection, radiation and aerosol-cloud interactions) [*Neale et al*., 2010a]. This is evident in the vertical profiles of aerosol extinction, which substantially differ from each other in different model versions (Figure 5). The cases using CAM4-BAM with MERRA winds (C4wf and C4wn) are in better agreement with CALIOP data [*Koffi et al*., 2012] compared to the other model versions tested here. Note that compared to the model physics (e.g., CAM4 versus CAM5), the new parameterization set results in second-order differences.

The seasonal cycle of dust AOD (Figure 7) shows a reasonable agreement with AERONET observations at most sites for the different model configurations (Table 4, O2), although the magnitude is not properly captured at all sites. The observed latitudinal shift in the positioning of the North African dust plume with the season [*Huneeus et al*., 2011] is captured by our model, as shown by the opposite seasonality displayed also for transatlantic transport by Northern stations such as Dahkla, Morocco, and Tamanrasset, Algeria compared to the southern stations such as Ilorin, Nigeria (Figure 7) and Surinam (not shown). We see an underestimation of AOD throughout the year at Ilorin, similar to most Aerocom models, whereas at Dahkla AOD from our CAM4 simulations is consistent with the AERONET retrievals, rather than overestimated [*Huneeus et al*., 2011].

Observations of the surface concentration (Figure 8) generally show a less smooth annual cycle than the AOD, and the correlation with the model is quite poor in many cases (Table 4, O5). The better performance in simulating the climatology of vertically integrated parameters such as AOD compared to surface

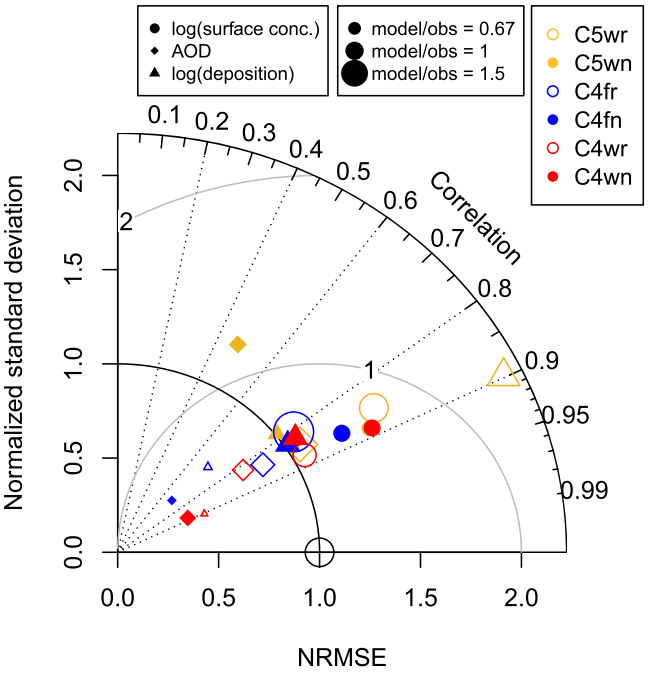

Figure 6. Taylor diagram showing the synthetic comparison of different model cases (see Table 3) to observations of average dust deposition, surface concentration, and AOD for current climate, shown in detail for the C4fn case in Figures 2–4 scatterplots (see Table 2). Note that a basic Taylor diagram does not show any information on the bias [*Taylor*, 2001], which we represent as a scale factor in the size of the plot symbols, proportional to the median of the model/observation ratio as reported in Table 4 (O6, O4, and O1). We use a logarithmic transform of the dust deposition and surface concentration variables, to account for the spread of the observed values over several orders of magnitude. Note that the symbol corresponding to C5wn surface concentration (yellow filled circle) is not visible as it is underlying the C4wn surface concentration (red filled circle).

concentration is a feature common to most global dust models [*Huneeus et al.*, 2011]. Note how in remote Pacific stations the new parameterizations (solid lines), in particular the wet deposition changes, reduces the overestimation in the peak season (Figures 8i–8l).

3.1.3. Dust Size Distributions

Observationally derived size distributions of dust in the atmospheric column from the dust-dominated AERONET sites provide a first-order constraint for this parameter close to the source areas. AERONET dust size retrievals rely on assumptions about the particles' shape and assume a bimodal size distribution [*Dubovik et al.*, 2006]. A known artifact is an overestimation of the submicron fraction [*Dubovik et al.*, 2000], so we do not include this size fraction here. For the supermicron fraction the AERONET retrievals show differences compared to other in situ observations [e.g., *Müller et al.*, 2012], showing either finer or coarser distributions, depending on the site and method they are compared to [*Maring et al.*, 2003; *Ryder et al.*, 2013]. This highlights the difficulty in estimating correctly the dust size distribution [*Reid et al.*, 2003; *Mahowald et al.*, 2013]. Nonetheless, we consider AERONET size retrievals for the selected stations a valuable source of information on dust size over the major dust sources, giving insights on the integrated vertical path.

The size distribution resulting from the new parameterization set undoubtedly shows a much improved fit to the data, both in the case of modeled and reanalysis winds (Figure 9). The evolution of dust size distribution deriving from medium to long-range transport is contrasted to observations from ice cores, by comparing dust deposition (Figure 10). In the case of medium-range transport (Asian ice cores) again there is a general improvement in representing the actual size distribution. For long-range transport (polar ice cores), the situation is more complicated. While some improvement may be due to the new parameterization set alone, model-data comparisons suggest that both an accurate representation of dust size (new parameterization) and meteorology (reanalysis winds) are necessary to obtain a good fit to the observations. The model (C4wn) also tends to simulate a transition to smaller particles too quickly in trans-Atlantic transport, when compared to in situ [*Maring et al.*, 2003; *Stuut et al.*, 2005] and sediment observations [*Mulitza et al.*, 2010] because of preferential settling by dry deposition [*Mahowald et al.*, 2013]. In general, the new parameterization set indeed provides a qualitatively more accurate representation of the dust size distribution and hence of the dust cycle.

3.1.4. Mass Balance

The magnitude or mass balance of the dust cycle for the "new" cases (Table 5) tends to show higher emissions and load and a shorter lifetime compared to the Aerocom median estimates of 1123 Tg/yr, 15.8 Tg, and 4.6 days, respectively [*Huneeus et al.*, 2011], consistent with our expectations from a coarser dust size. The results for C4fn (2827 Tg/yr, 23.8 Tg) and C4wn (2002 Tg/yr, 17.8 Tg) are within the Aerocom models range for dust emissions and load, respectively, whereas for C5wn (8226 Tg/yr, 42.6 Tg) they are larger. Dust

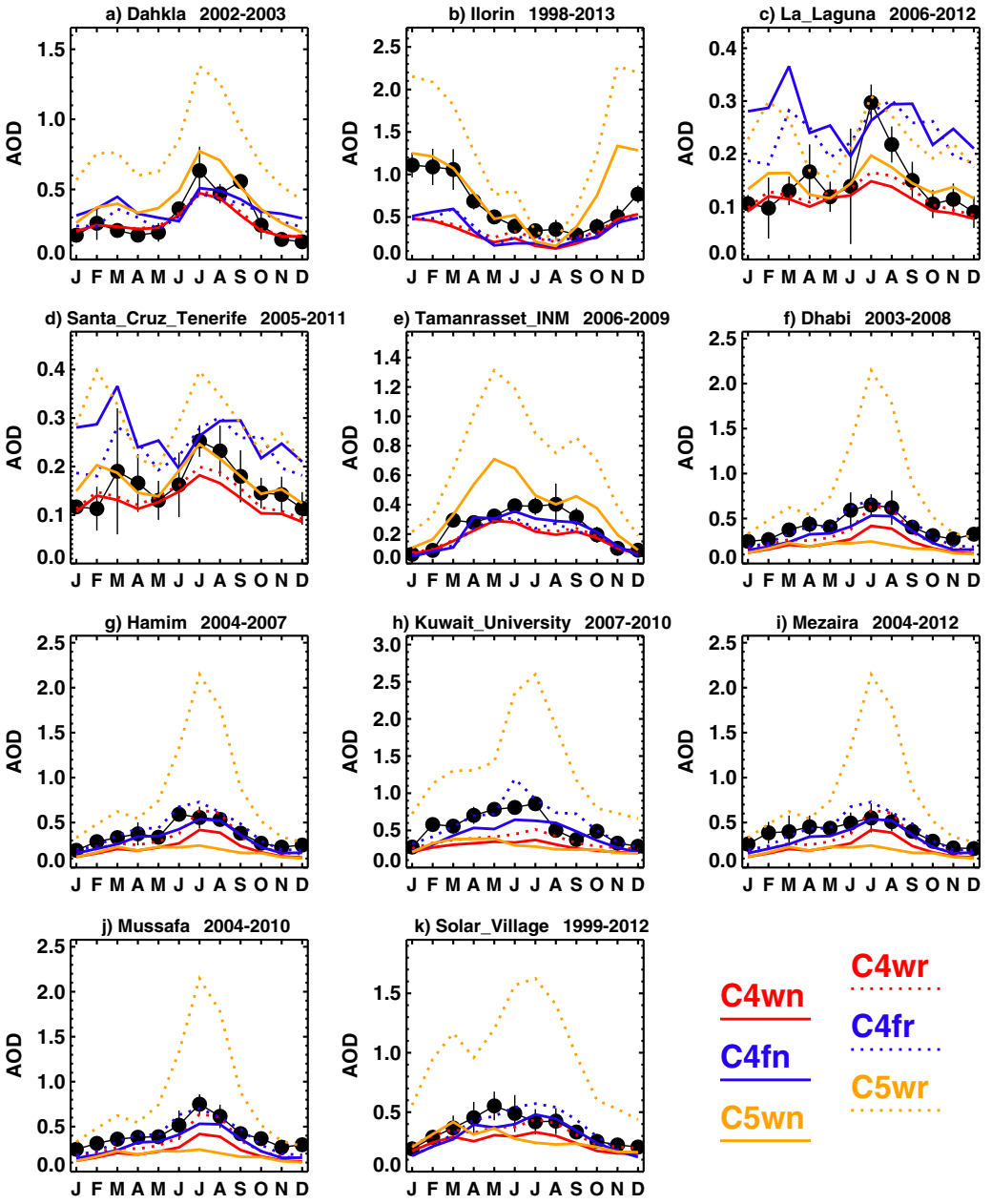

Figure 7. Comparison of model and observation for the annual cycle for AOD. Observations are from AERONET stations [*Holben et al.*, 1998].

lifetimes instead are within the Aerocom model range for all cases (Table 5). Interannual variability (1 standard deviation) is less than 10% for all the metrics (Table 5). The much larger magnitude of dust emissions (8x) and load (4x) of C5wn compared to the Aerocom median does not imply a significantly worse overall performance of this particular model relative to the others (e.g., C4fn and C4wn) when compared to the observations (Table 4), thus suggesting that the uncertainty in constraining the magnitude of the dust cycle—hence its climate and biogeochemical impact—is still large.

Noteworthy are the differences in dust lifetimes among different cases, in particular for CAM4 versus CAM5. For the latter, the short aerosol lifetimes are attributed to the large wet removal rate (+60% compared to the Aerocom mean), also due to internal mixing with more hygroscopic species [*Liu et al.*, 2012].

Significant differences (shortening) in dust lifetimes emerge between the "old" and "new" parameterization sets (Table 5; C4fr, C4wr versus C4fn, C4wn). The sensitivity runs that isolate the effects of dust optical

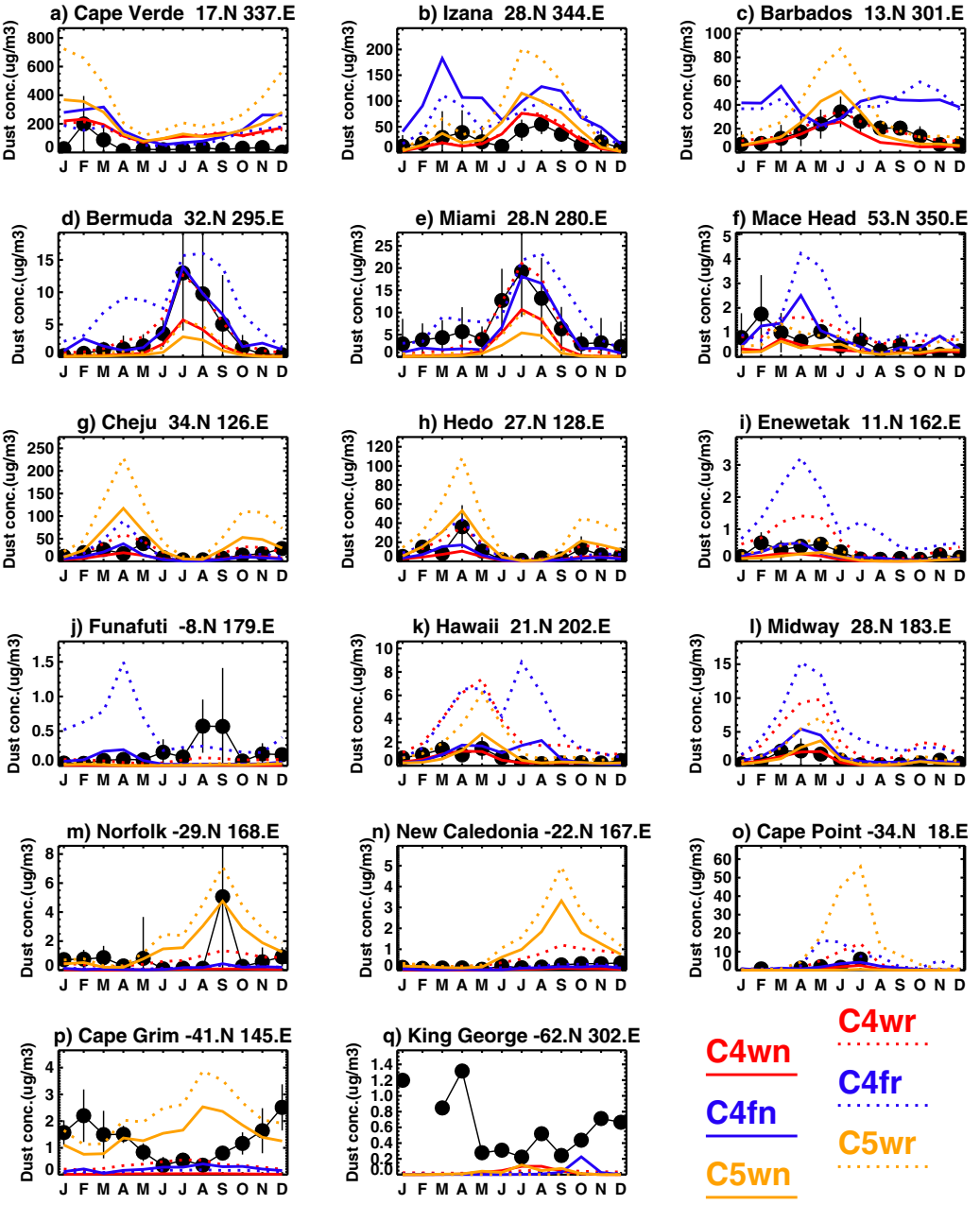

Figure 8. Comparison of model and observation for the annual cycle for dust surface concentration ($\mu g/m^3$). Observations are from *Prospero et al*. [1989].

properties (C4fn-ro) and size distribution (C4fn-rs) do not show large variations in lifetimes compared to C4fn, suggesting that wet deposition is the primary factor in controlling the shortening of dust lifetimes. A secondary factor could be the new size distribution (in fact C4fn-rs has the larger lifetimes of all C4fn cases), consistent with our shift of mass away from the smallest size bin. This is also evident in the vertical profiles of aerosol extinction, with the tendency of "new" parameterization dust to shift at lower levels compared to the release versions (Figure 5). Finally, the "tuning" of the source areas could be putting more dust in places where the model simulates a wetter climate.

3.2. Last Glacial Maximum Dust

The Last Glacial Maximum is a time period with 2–3 times more dust than in the current climate globally [e.g., *Kohfeld and Harrison*, 2001; *Maher et al*., 2010]. Previous modeling studies have compiled data sets and created climatologies for this time period [e.g., *Mahowald et al*., 1999; *Mahowald et al*., 2006b]. Here we

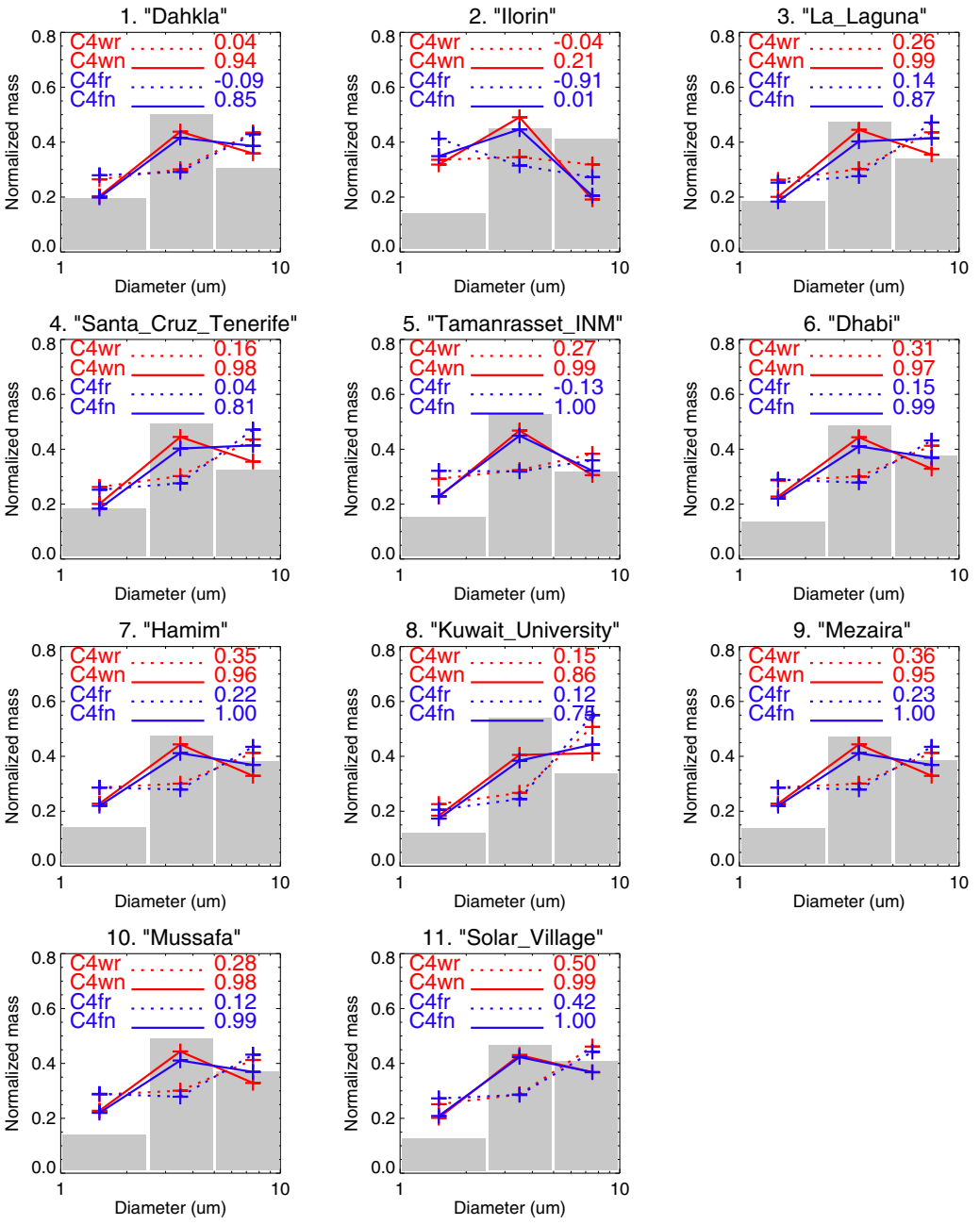

Figure 9. Comparison of model and observation for dust size distributions in the 1–10 μm range. Observations are from AERONET stations [*Dubovik and King*, 2000]. Correlation coefficients between model and observations across the three size bins are reposted for each case.

repeat the previous analysis with our new model version to contrast the results. In the case of the LGM simulation (C4fn-lgm), the magnitude of the tuned modeled dust deposition is representative of the paleodust observations in most cases, over the 4 orders of magnitude spanned by the data (Figure 11). Dust emissions are 6289 Tg/y, about 2.2 times the current estimate with C4fn (Table 5). About 20% of the emissions come from the glaciogenic sources, which is less than the 1/3 in the CAM3 simulations [*Mahowald et al*., 2006b]. The LGM/current ratio for dust load (1.6) is smaller than the emissions ratio, because of a shorter lifetime, which is higher (2.2 versus 2.0 days) than *Mahowald et al*. [2006b]. Although the dust load is much lower (37.4 versus 77 Tg/y), the LGM/current ratios for CAM4 are very similar to CAM3 [*Mahowald et al*., 2006b] for emissions, load, and lifetimes. The magnitude of the dust cycle in terms of dust load is also higher than other model estimates, that indicate, respectively, 23 $\pm$ 14 Tg [*Werner et al*., 2002] and 30.84 Tg [*Takemura*

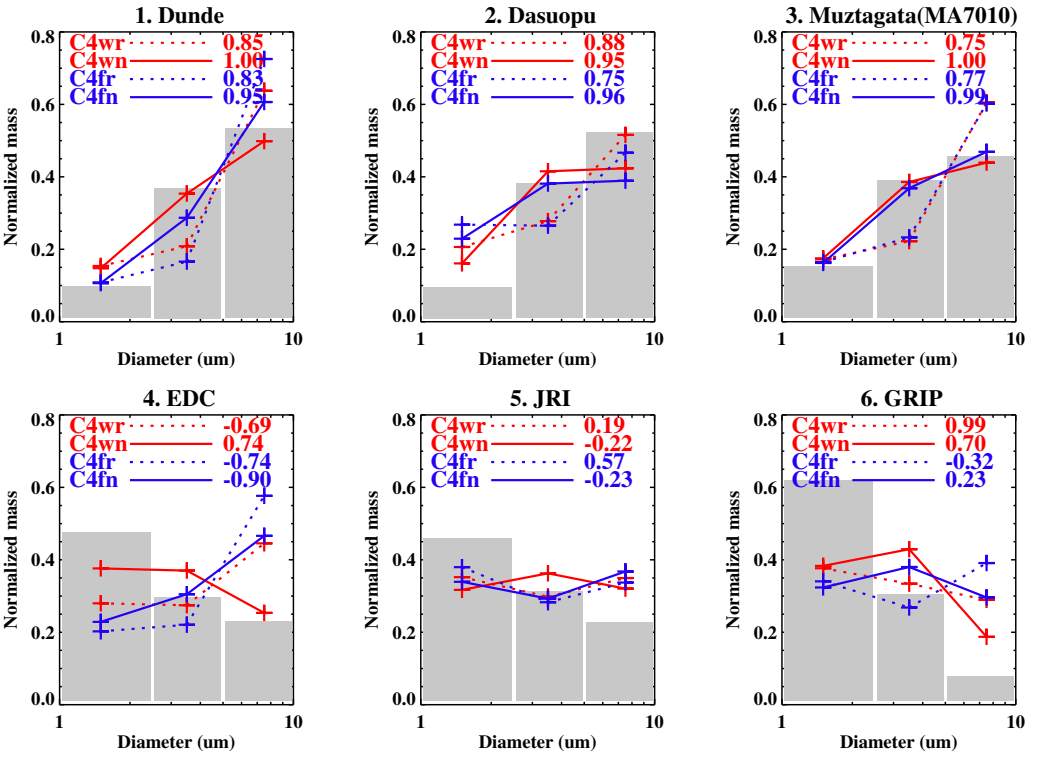

Figure 10. Same as Figure 8 for dust deposition. Observations are from ice cores [*Delmonte et al*., 2004; *Steffensen*, 1997; *McConnell et al*., 2007; *Wu et al*., 2009].

et al., 2009], with larger LGM versus current/preindustrial ratios (2.39 and 2.8, respectively, compared to our 1.6). This is in line with opposite trends for dust lifetimes, which are decreasing in the LGM in our simulations but increase in *Werner et al*. [2002]. Compared to *Lunt and Valdes* [2002], our LGM versus current increase in dust load is larger (1.6 versus 1.39), although in their simulations lifetimes are almost unchanged with climate and are much longer than ours (5.5 days). In terms of AOD our simulation indicates a much smaller value (0.038 versus 0.14) than *Claquin et al*. [2003], as for the LGM/current ratio (1.6 versus 2.8).

In a hypothetical case, using the same model but switching to a coarser size distributions for the emissions (like previous studies, e.g., *Mahowald et al*. [2006b]) would cause a decrease in the dust lifetime. From a global budget perspective, a model with a relatively coarse size distribution at emissions (such as ours) would tend to have lifetimes dominated by the quick removal of coarse particles, hence relatively short lifetimes. The decrease in lifetimes in our simulation is related to a reduced lofting in the LGM versus current (Figure S6), similar to what was seen in the CAM3 [*Mahowald et al*., 2006b; *Albani et al*., 2012b]. In addition, there is a shift of the sources toward higher latitudes, where the planetary boundary layer height is lower and decreases in glacial climate (Figure S6). These combined effects result in a ∼22% decrease in dust dry deposition lifetime. The spatial features highlight the large decrease in lifetime close to the main dust sources (Figure S7). On the other hand, a drier LGM climate—which is also simulated in our model [*Brady et al*., 2013], does not necessarily imply increased wet deposition lifetimes, since wet deposition largely depends on precipitation frequency rather than amount in our model [*Mahowald et al*., 2011]. In fact we see a ∼18% decrease in dust wet deposition lifetime. Spatially explicit calculation of the lifetime suggests that large wet deposition in the midlatitudes close to the expanded glacial sources contribute strongly to reduced dust wet lifetimes as well (Figure S8). This is consistent with the idea that periglacial sources tend to be situated in moister regions compared to the desert dust sources (otherwise they would be considered desert dust sources). The dominant places which display longer wet deposition lifetimes are over very high latitude regions where the very low precipitation (and precipitation frequency) becomes important (e.g., Figure S7) [*Mahowald et al*., 2011; *Albani et al*., 2012b].

Table 5. Diagnostics of the Global Dust Cycle for Different Model Cases and Relative Percent Variability (1 Standard Deviation), Representing the Multiyear Average and Interannual Variability

Case	Emissions (Tg/y) (%)	Load (Tg) (%)	Lifetime (d) (%)	AOD (%)
C4fr	2365 ± 3.8	27.5 ± 4.4	4.2 ± 1.6	0.032 ± 4.7
C4fn	2827 ± 5.8	23.8 ± 4.6	3.1 ± 2.1	0.024 ± 5.1
C4wr	2122 ± 5.7	26.4 ± 4.3	4.6 ± 2.4	0.029 ± 4.5
C4wn	2002 ± 5.9	17.8 ± 4.3	3.3 ± 4.1	0.018 ± 4.6
C5wr	15687 ± 5.8	78.8 ± 5.3	1.8 ± 3.0	0.088 ± 5.2
C5wn	8626 ± 6.0	42.6 ± 5.7	1.8 ± 3.6	0.041 ± 5.7
C4fn-rs	2855 ± 1.6	26.8 ± 0.8	3.4 ± 0.8	0.036 ± 0.9
C4fn-ro	2563 ± 2.2	23.2 ± 4.8	3.3 ± 2.6	0.018 ± 4.8
C4fn-s2	2743 ± 10	26.3 ± 5.4	3.5 ± 4.6	0.026 ± 5.9
C4fn-lgm	6289 ± 3.6	37.4 ± 5.4	2.2 ± 1.4	0.038 ± 4.0
C4fn-lgm-s2	6705 ± 4.2	42.4 ± 5.6	2.3 ± 1.3	0.045 ± 6.4

3.3. Dust Radiative Forcing

Dust Radiative Forcing (RF) is calculated as the difference between the radiative forcing of all aerosol species and a calculation including all aerosols except dust, and is calculated online in the model by calculating the radiation multiple times for each time step.

The refined parameterization set described in the previous sections produced changes in dust RF in the "new" cases simulations compared to the release versions of the model. We compare both pairs with estimates, based on satellite-derived observations, of radiative forcing efficiency, based on clear-sky dust Top Of the Atmosphere (TOA) RF over the North Atlantic [*Li et al*., 2004] and the Sahara [*Zhang and Christopher*, 2003; *Patadia et al*., 2008] (Table 6). The new cases are in better agreement with observations, not only as obviously expected for the LW (which was ignored for the release version of CAM4) but also for the SW RF, especially over Sahara [*Patadia et al*., 2008]. For our comparison, we ignore the estimates over the North Atlantic for the "low" dust season (DJF), which are probably contaminated by biomass burning aerosols as indicated by the low single scattering albedo [*Li et al*., 2004].

An accurate partitioning of solar absorption between atmosphere and the surface, often not achieved by climate models, is also important [*Miller et al*., 2004; *Wild*, 2008]. Estimates of surface RF efficiency, i.e., the broadband SW radiative forcing per unit AOD at 550 nm (-65 W/m^2) over the North Atlantic by *Li et al*. [2004] are in good agreement with C4fn (-69 W/m^2), which is an improvement over C4fr (-93 W/m^2).

The combination of absorption and reflection of solar radiation caused by the dust burden leads to a negative SW RF at the surface, centered over and downwind of the major (and high albedo or "brighter") desert (North Africa and Arabian peninsula) dust sources (Figure 12), with absorption causing a positive atmospheric column SW RF. The balance at the TOA is generally a slightly positive SW RF right above the major dust sources and a negative SW RF elsewhere (Figure 12a). The absorption and re-emission of radiation by dust in the LW spectrum causes a positive RF at surface, associated with a negative atmospheric LW RF. At the TOA there is a slightly positive LW RF (Figure 12b). Resulting from both SW and LW contributions, the net balance shows a generally positive net RF in the atmosphere, whereas a somewhat similar structure at the surface and at the TOA shows, respectively, a null and a slightly positive net RF over the major desert dust sources and a negative net RF everywhere else (Figure 12c). This spatial pattern is similar to a study using similar optical properties [*Balkanski et al*., 2007].

A roughly similar spatial pattern is seen in the cases using reanalysis winds and/or a different version of the model, as also indicated by similarity in the features of the zonally averaged net RF (Figures 13a–13c). Nonetheless, the area characterized by a RF markedly different from zero is less pronounced (both spatially and in magnitude) in the C4wn, but is more pronounced in the C5wn case than in C4fn (Figures 13a–13c). Accordingly, this results in a more negative TOA RF globally for C4fn (-0.23 ± 0.02 W/m^2) compared to C4wn (-0.08 ± 0.01 W/m^2), whereas C5wn has the more negative balance (-0.29 ± 0.02 W/m^2) (Table 7). When accounting for the dust mass balance in each case, i.e., if we scale those values by unit AOD, we see different RF efficiencies, with C4fn displaying the highest RF efficiency (Table 7). Compared to the new versions of the model, dust in CCSM3 experiments had a larger TOA net RF (-0.61 W/m^2 in *Yoshioka et al*. [2007] and -0.46 W/m^2 in *Mahowald et al*. [2006c]), mostly due to the offsetting effects of the SW and LW over land versus ocean surface [*Yoshioka et al*., 2007], and a strong negative balance in the atmosphere

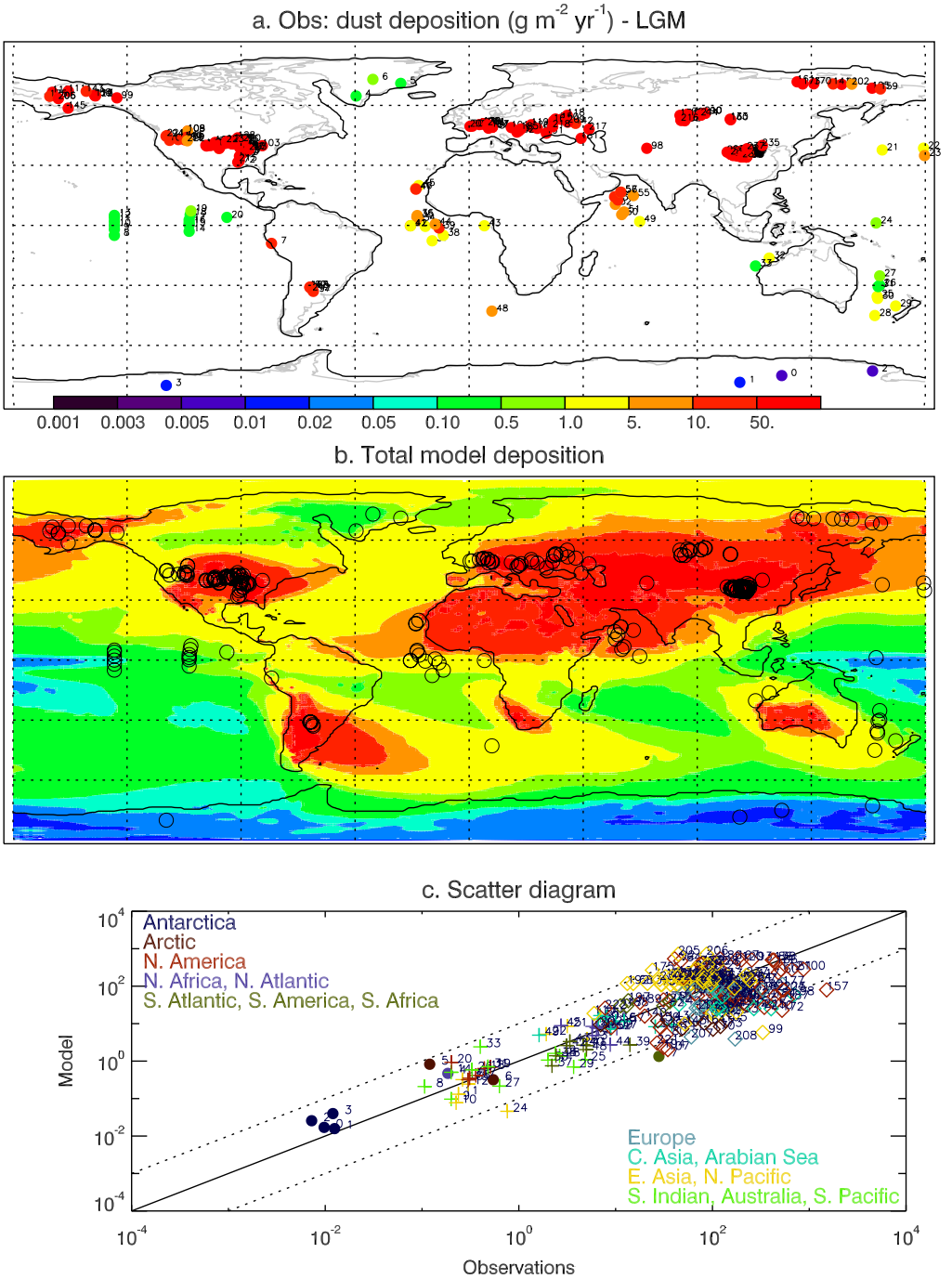

Figure 11. Same as Figure 2 for the Last Glacial Maximum.

over North African and Asian dust sources (Figures 13d–13f, solid lines). The main source of the difference between CCSM3 and these results (which use similar optics) come from the prescribed coarser size distribution here (Figure 13g, C4fn-rs case versus C4fn-rs and Figure 13d, C3). Overall our net dust TOA RF is within the range of estimates from other models (Figure 14), showing a negative RF.

In the LGM simulation (C4fn-lgm), the zonally averaged distribution of surface RF, similar to C3-lgm [*Mahowald et al.*, 2006b], resembles the geographical distribution of the main dust sources, including the mid/high-latitude glaciogenic sources in both hemispheres, but shows a slight decrease compared to C4fn over

Table 6. Comparison of Observed and Modeled Net TOA Clear-Sky RF (W/m^2)

Parameter	SW TOA JJA	LW TOA Sept	SW TOA JJA
Domain	N. Atlantic 15°N–25°N, 45°W–15°W	Sahara 15°N −35°N, 18°W–40°E	Sahara 15°N–35°N, 18°W–40°E
Reference	*Li et al.* [2004]	*Zhang and Christopher* [2003]	*Patadia et al.* [2009]
Obs.	-35 ± 3	15	∼0 for Albedo of 0.40
C4fr	-31.7 ± 0.4		18.4 ± 0.4
C4fn	-34.5 ± 0.2	9.8 ± 0.6	3.1 ± 0.3
C4wr	-28.4 ± 0.7		19.9 ± 0.7
C4wn	-32.4 ± 0.8	9.2 ± 0.3	3.6 ± 0.4
C5wr	-21.4 ± 1.1	4.0 ± 0.3	11.9 ± 0.9
C5wn	-32.2 ± 1.0	5.0 ± 0.4	-1.1 ± 0.3
C4fn-ro	−24.36		30.05
C4fn-rs	−32.82	7.52	−0.56
C4fn-s2	−33.63	9.39	2.33

the desert areas centered at 15°N (Figure 13f). The net atmosphere RF is positive and, as for current climate, does not show a contrasted net RF balance depending upon the underlying surface being land or ocean, as was the case for CAM3 (Figure 13h versus *Mahowald et al.* [2006c]). The balance at the TOA resembles the surface features, except it shows a positive net RF at Northern high latitudes, similar to C3-lgm (Figure 13d), due to the relatively high positive atmosphere SW RF (Figure S9). Those areas correspond to bright surfaces with high albedo, such as the sea ice covered Arctic Ocean and the southern margins of the Laurentide and Fenno-Scandian Ice Sheets, close to the major North American and European dust sources (Figure S9). A positive high-latitude TOA RF was also simulated by previous work [*Overpeck et al.*, 1996; *Claquin et al.*, 2003], although those studies showed a different spatial pattern of the Northern Hemisphere dust burden than our model, centered at higher and lower latitudes, respectively.

The average global net TOA RF for C4fn-lgm is -0.32 ± 0.01 W/m^2, which is smaller than the C3-lgm estimate (-1.61 W/m^2), as a result of an almost halved dust load, and to a lesser extent to a lower RF efficiency. This value is much smaller than other model-based estimates (-3.2 and -3.3 ± 0.8 W/m^2, respectively) by *Claquin et al.* [2003] and *Chylek and Lohmann* [2008], but is larger than the *Takemura et al.* [2009] estimate of -0.02 W/m^2 (Figure 14). Simpler estimates extrapolated from ice cores data suggest an intermediate value of -1.9 ± 0.9 W/m^2 [*Köhler et al.*, 2010]. The LGM/current ratio for the net TOA RF is 1.4, which is lower compared to the 3.5 from the previous estimates from *Mahowald et al.* [2006c] and *Claquin et al.* [2003]. In view of this fact, the smaller net TOA dust RF simulated in the LGM by our model is consistent with a smaller value also simulated for the current climate. Given that the optical properties were similar for both models, a coarser size distribution in CAM4 compared to CAM3 possibly implies a somewhat smaller dust SW RF, see section 4.1 and Table 7, that shows how using the release (finer) size distribution yields an increase in dust net TOA RF of a factor ∼2 in current climate (C4fn versus C4fn-ro), as discussed more below. The coarser size distribution in CAM4 also impacts the RF balance indirectly by decreasing dust lifetime. In addition, surface dust-snow interactions reducing surface albedo are simulated in CAM4 [*Flanner et al.*, 2007], although the effects of dust deposition onto snow (in contrast to black carbon) tend to be small in this model (Figure S10).

4. Discussion

4.1. Model Sensitivity

In this section we discuss the model's sensitivity to changes in dust size and optics, disentangling at the same time the impacts that each one has on RF in the new version (C4fn) (e.g., similar to *Miller et al.* [2004]).

The sensitivity study highlights the effects on the dust RF caused by the changes in dust size and optical properties (Table 7 and Figure 13). The new optical properties yield a reduced difference in absorbed energy between the surface and atmosphere, due to reduced SW atmospheric absorption and the inclusion of LW cooling of the atmosphere (and warming of the surface), in similar proportions (Table 7 and Figures 13h and 13i: C4fn versus C4fn-SW compared with C4fn-ro versus C4fn-SW, which is just the SW component from C4fn). On the other hand, the new dust size distribution causes a slight reduction in the surface-atmosphere energy gradient as a consequence of decreased SW surface cooling (Table 7 and Figures 13h

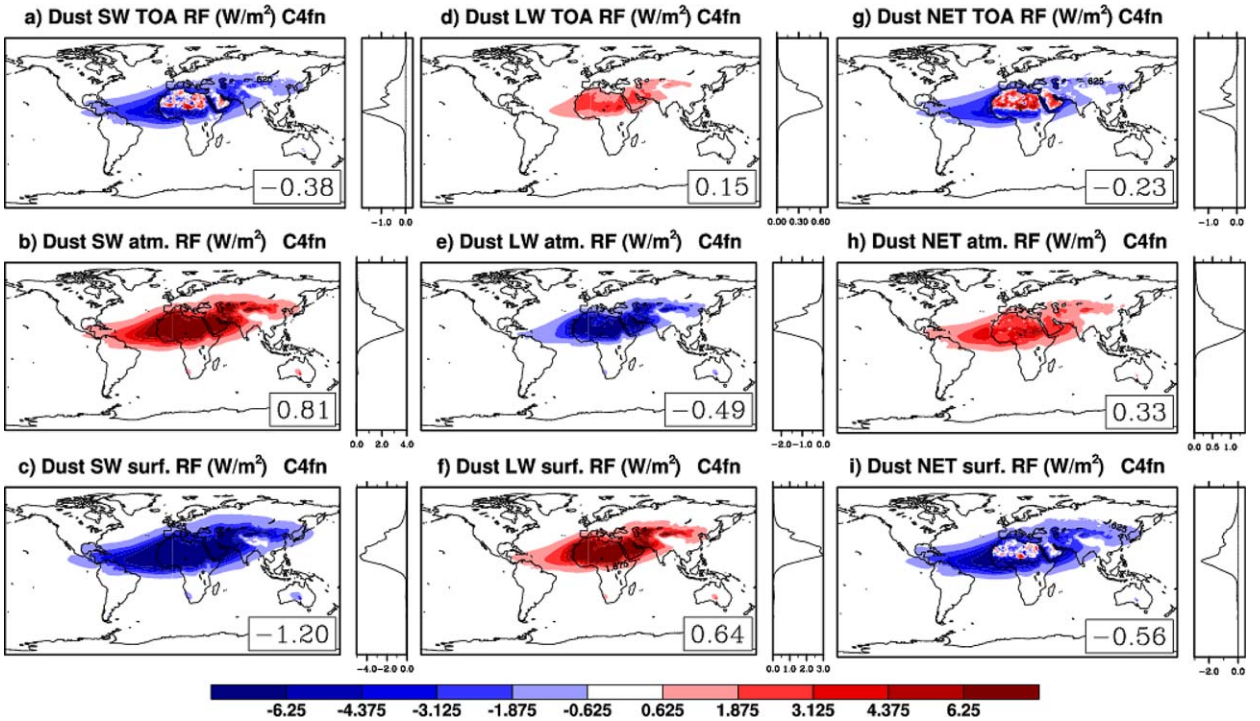

Figure 12. Dust radiative forcing (W/m^2) for the C4fn case. (left) SW RF; (middle) LW RF; (right) net RF. (top) TOA; (middle) atmospheric column; (bottom) surface. Right plots associated to each map represent the zonal averages of dust net RF.

and 13i: C4fn versus C4fn-rs and C4fn-SW versus C4fn-rs-SW). The effects of the new optical properties (e.g. −59% and −76% for absolute values of net surface and atmosphere RF, respectively) are larger than those related to the new size distribution (−29% and −3%) in quantitative terms (W/m^2) (Table 7). Finally, Figures 13g–13i (C4fn-ro versus C4fn-SW) clearly shows that while at the surface the inclusion of LW-dust interactions tends to balance the surface cooling, the larger differences in the net radiative budget are in the atmosphere linked to the reduced SW absorption, which is what drives the difference in the TOA energy balance (Table 7 and Figure 13g: C4fn versus C4fn-SW versus C4fn-ro). Interestingly, the differences in balance between the surface and atmosphere net RF result in estimates of the net TOA RF of different magnitude and even sign, with old optical properties (C4fn-ro) resulting in a small positive forcing (+0.02 W/m^2) and old size distribution (C4fn-rs) giving a larger negative forcing (−0.45 W/m^2) compared to C4fn (−0.23 ± 0.02 W/m^2) (Table 7).

Comparing the net RF for C4fn and C4fr shows that at TOA the net global balance is similar for the two cases (−0.23 ± 0.02 versus −0.28 ± 0.01 W/m^2), which also have almost the same RF efficiency (Table 7). Nonetheless, while the spatial patterns of net TOA RF look rather similar around the main dust sources, C4fr shows a positive RF over the Arctic (Figure 13g). The anomalous RF at Northern high latitudes in C4fr is likely due to the stronger long-range transport to the Arctic of dust aerosols compared to the other cases. The net surface RF of all our simulations (C4fn: −0.56 ± 0.03 W/m^2; C4wn: −0.32 ± 0.02 W/m^2; C5wn: −0.74 ± 0.04 W/m^2; Table 7) are also smaller than other models that use comparable optical properties [e.g., *Sinyuk et al.*, 2003], with estimates of −0.82 W/m^2 [*Miller et al.*, 2006] and −0.92 W/m^2 [*Balkanski et al.*, 2007].

Subtle differences in prescribing the submicron fraction at the emission result in large differences in its relative proportions when it comes to the atmospheric dust load (because of the size selection process during transport), hence AOD (Figure 15) and RF (submicron particles are the most effective scatterers). In addition the relative importance of the submicron fraction is poorly constrained by observations across large spatial scales [*Mahowald et al.*, 2013]. Based on those considerations, we also conducted a sensitivity test (C4fn-s2) with a slight variation on *Kok* [2011] size distribution, in order to double the relative contribution of model bin1 (0.1–1 μm) to the emissions. We compare model size distributions with observations for long-range

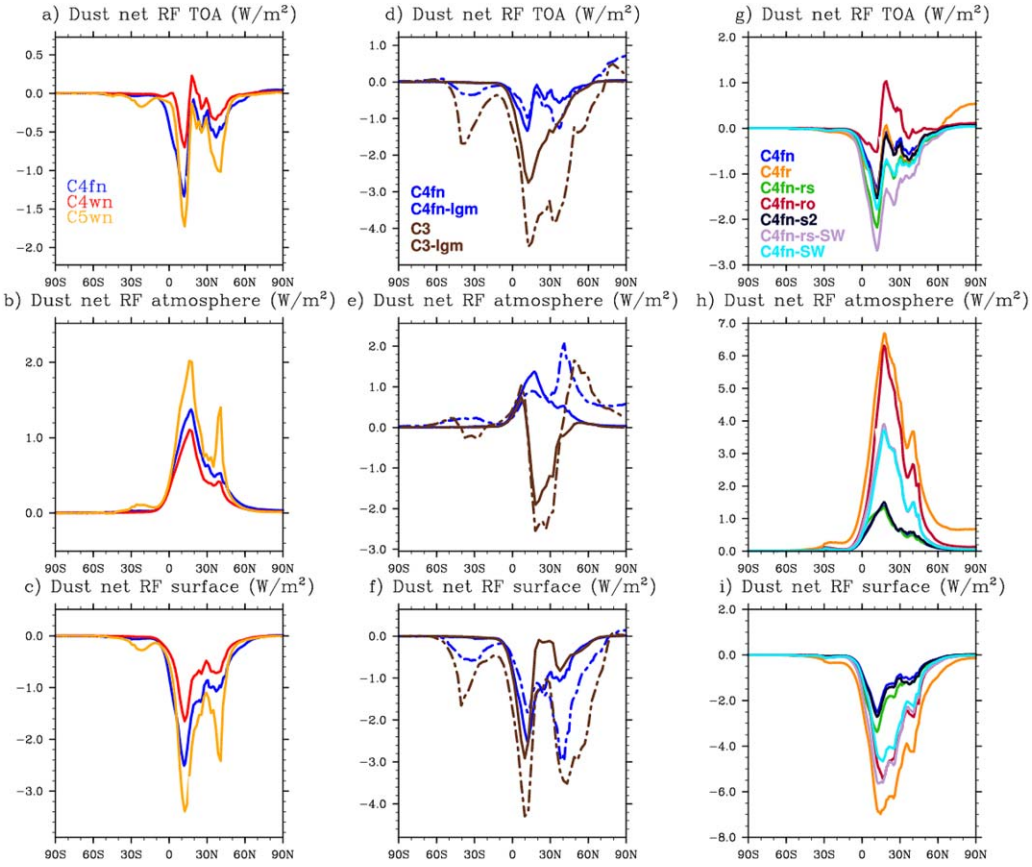

Figure 13. Zonal averages of dust radiative forcing (W/m^2) for different model cases. Figures 13a–13c compare C4fn, C4wn, and C5wn cases for net RF. Figures 13d–13f compare C4fn, C4fn-lgm, C3 and C3-lgm for net RF. Figures 13g–13i compare C4fn, C4fr, C4fn-rs, C4fn-ro, C4fn-s2 cases for net RF and C4fn-rs (C4fn-rs-SW) and C4fn (C4fn-SW) cases for the SW component of RF. (a–g) TOA; (b–h) atmospheric column; (c–i) surface. C4fn-SW identifies the SW component alone of the C4fn simulation.

transport (Table 8; see also section 4.2). While there are large uncertainties even in the observations, it is clear that the model underestimates the submicron fraction at the remote sites, even in the case using reanalysis winds (C4wn) which performs better, similar to what we discussed for the supermicron fraction (Figures 9 and 10). Assuming that the size distribution for the emissions is consistent with the observations [*Kok*, 2011] (Figure 7), other modeled processes affecting either size sorting during transport or at the deposition sites are responsible for the underestimation [*Mahowald et al.*, 2013].

The spatial distribution pattern of net RF, when we include more small particles, looks similar to the base case (C4fn-s2 versus C4fn) (Figures 13g–13i), with a slightly higher negative global net TOA RF (−0.28 W/m^2). This is associated with a higher RF efficiency than C4fn, but much lower than that of the release size

Table 7. Globally Averaged Dust Loading (Tg), Radiative Forcing at TOA, Atmosphere and Surface and Variability (1 Standard Deviation) (W/m^2), and RF Efficiency (W/m^2 Gg)

Case	Load (Tg)	Net RF TOA	Net RF Atm.	Net RF Surf.	SW RF TOA	SW RF Atm.	SW RF Surf.	Net RF TOA/Load	SW RF TOA/Load
C4fr	27.5	−0.28 ± 0.01	1.85 ± 0.09	−2.13 ± 0.10	−0.28 ± 0.01	1.85 ± 0.09	−2.13 ± 0.10	−8.6	−8.6
C4fn	23.8	−0.23 ± 0.02	0.33 ± 0.01	−0.56 ± 0.03	−0.38 ± 0.02	0.81 ± 0.04	−1.20 ± 0.06	−8.8	−12.8
C4wr	26.4	0.02 ± 0.01	1.72 ± 0.07	−1.70 ± 0.07	0.02 ± 0.01	1.72 ± 0.07	−1.70 ± 0.07	4.8	4.8
C4wn	17.8	−0.08 ± 0.01	0.25 ± 0.01	−0.32 ± 0.02	−0.18 ± 0.01	0.61 ± 0.03	−0.79 ± 0.03	−0.9	−4.9
C5wr	78.8	0.18 ± 0.02	2.79 ± 0.12	−2.61 ± 0.11	−0.05 ± 0.02	3.80 ± 0.16	−3.85 ± 0.16	8.6	4.7
C5wn	42.6	−0.29 ± 0.02	0.45 ± 0.03	−0.74 ± 0.04	−0.43 ± 0.03	1.01 ± 0.05	−1.44 ± 0.08	−4.7	−10.5
C4fn-rs	26.8	−0.45	0.34	−0.79	−0.61	0.88	−1.49	−16.8	−22.9
C4fn-ro	23.2	0.02	1.38	−1.36	0.02	1.38	−1.36	0.8	0.8
C4fn-s2	26.3	−0.28	0.34	−0.62	−0.44	0.85	−1.28	−10.6	−16.6
C4fn-lgm	37.3	−0.32 ± 0.01	0.50 ± 0.02	−0.82 ± 0.03	−0.55 ± 0.02	1.24 ± 0.05	−1.79 ± 0.06	−8.5	−14.6
C4fn-lgm-s2	42.4	−0.41	0.54	−0.95	−0.65	1.32	−1.97	−9.7	−15.4

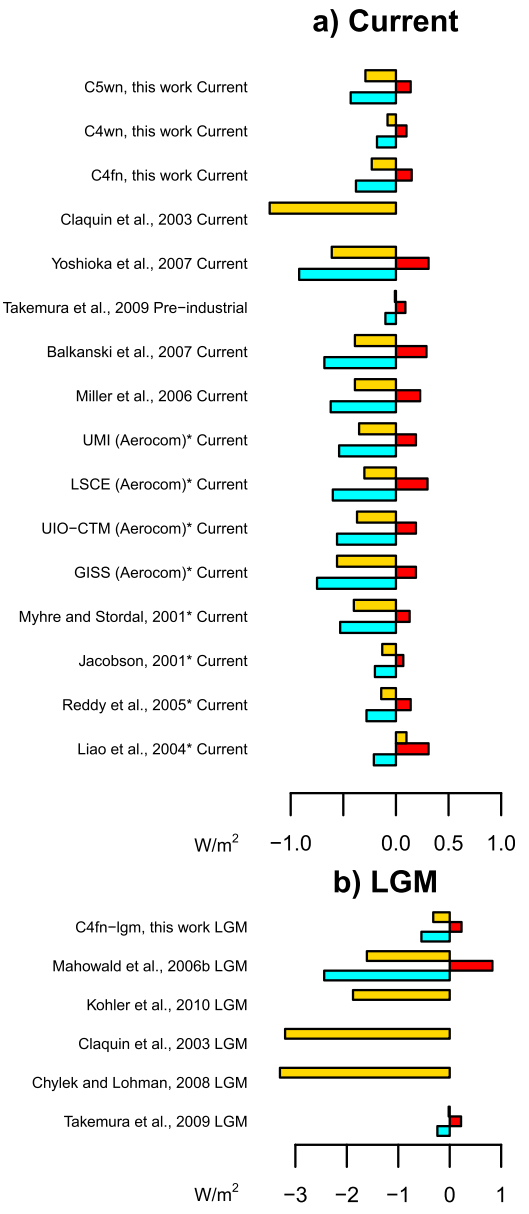

Figure 14. Comparison of dust TOA RF estimates (W/m^2) for current and LGM climates from our results and from the literature (asterisk = reported from IPCC AR4), partitioned in net (yellow bars), LW (red bars), and SW (cyan bars) RF.

distribution (C4fn-rs) (Table 7), in line with the relative proportions of small particles (Figure 15). The size sensitivity case for the LGM (C4fn-lgm-s2) shows a RF spatial pattern (Figure S11) similar to C4fn-lgm (not shown), whereas the global net TOA RF is, respectively, −0.32 and −0.41 W/m^2, again indicating a higher but not huge RF efficiency for the case "enriched" in finer dust (Table 7), suggesting that the radiative forcing is sensitive to the contribution of submicron dust to the dust load.

In general, the spread of the RF plots from Figures 13g–13i shows how variations in individual aspects of the modeled dust cycle have a large impact on RF (Figures 13d–13f), highlighting the importance of details of the size and optics in modeling [e.g., *Miller et al.*, 2004].

4.2. Discussion of the Uncertainties

The major source of uncertainty in dust models is represented by the magnitude and location of the emissions [e.g., *Cakmur et al.*, 2006; *Shao et al.*, 2011; *Huneeus et al.*, 2011]. To overcome this limitation some tuning of model emissions is still necessary. As already described, we achieved this by optimizing the soil erodibility maps to give best fit to the observations.

To estimate the uncertainty associated with the particular choice of the observational data set, we compare two cases where just the optimization algorithm was used [*Mahowald et al.*, 2006b], without further refining. In the first case the bulk value of Mass Accumulation Rates (dust deposition flux) was used, in the second case we considered only the fraction $<$10 μm, consistent with our model size range (Figure S12). Failing to match the observational and model's size range can yield a difference of ∼20% in AOD estimates globally (Table 9).

In general, large uncertainties still exist on both the fine and coarse dust size range we consider in our model. Our parameterization assumes that dust is emitted only through the mechanism described by *Kok* [2011], and within that framework we chose to limit our size to particles with diameters smaller than 10 μm. Airborne dust particles larger than 10 μm, despite the uncertainties in the measurement techniques [*Reid et al.*, 2003], have indeed been observed both over the major dust sources [*Reid et al.*, 2003; *Ryder et al.*, 2013] and over the sea in the North African continental margin [*Stuut et al.*, 2005], but they have been observed to decrease during transport across the Atlantic Ocean [*Maring et al.*, 2003]. On the other hand,

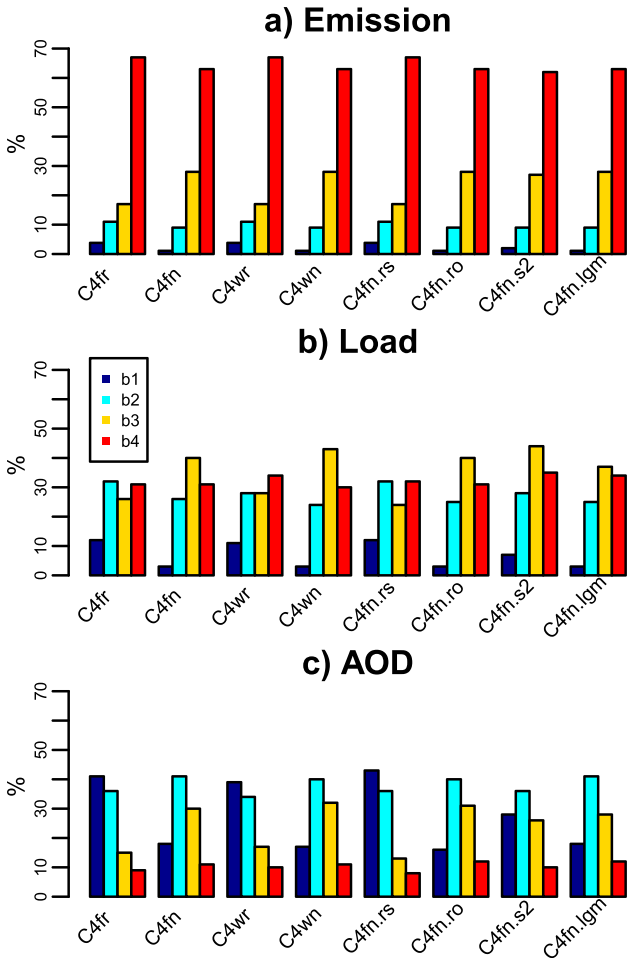

Figure 15. Relative proportions (%) of dust (a) emissions, (b) load, and (c) AOD for different simulations in the four model bins: b1 (blue), b2 (cyan), b3 (yellow), and b4 (red).

on the lower side of our size range, our sensitivity study highlighted the potential for large uncertainties in dust RF from small, poorly observed dust particles. Observations in this size range are challenging [*Reid et al.*, 2003], but in general our model simulations tend to underestimate the submicron fraction far from the source areas (Table 9), despite the fact that the match with the very same set of observations in the 1–10 μm (where the observations are more reliable) is good (Figure 10), at least with reanalysis winds (C4wn).

Another interesting outcome is the indication that the case using reanalysis winds (C4wn) has a better ability to reproduce the evolution of size distribution with a shift toward finer particles with long-range transport (Figure 10 and Table 1). This may be connected to the spatial features of RF, which seems to suggest that the model winds (C4fn) tend to be more conducive to mass transport (and associated RF) far from the source areas than the reanalysis winds (C4wn and C5wn) (Figures 13a–13c), likely through the larger dust bins (Figure 10). This would explain the lower RF efficiency of C4wn and C5wn then C4fn (Table 7). The vertical profiles of aerosol extinction confirm this hypothesis, as shown by the higher-level peak of the C4f cases than those using reanalysis winds (Figure 5). Problems with the model vertical mixing become apparent in the inconsistency between the high bias of modeled surface concentrations compared to the low bias of deposition (Figure 6), as well as by looking at the seasonal cycle simulated at Barbados (Figure 8). There the C4fn (but not C4wn or C5wn) fails to reproduce the observations of dust concentration at the surface (Figure 8), but the modeled seasonal cycle higher up in the model (e.g., 2–3 vertical levels higher) does mimic the surface observations (not shown).

4.3. Quantification of the Uncertainties

The reference experiments for our estimates of TOA RF are the C4fn for current climate and C4fn-lgm for the LGM. We consider three synthetic parameters to give a quantitative estimate of the uncertainty

Table 8. Comparison of Observed and Modeled Relative (%) Amount of Dust in Model bin1 (0.1–1 μm)

Site	Reference	Observations	C4fn	C4fn-s2	C4wn
EDC	*Delmonte et al.* [2004]	7.4	2.9	6.1	5.2
JRI	*McConnell et al.* [2007]	21.9	4.8	6.2	5.0
GRIP	*Steffensen* [1997]	15.3	4.3	6.1	5.2
Dunde	*Wu et al.* [2009]	0.2	1.3	2.5	1.9
Dasuopu	*Wu et al.* [2009]	0.2	3.0	6.1	2.0
Muztagata(MA7010)	*Wu et al.* [2009]	0.6	2.0	3.0	2.2

Table 9. Comparison of Simulations Where With Soil Erodibility Constrained by Observations of Bulk Deposition (Full Size Range) Versus the Fraction <10 μm

	Emission (Tg/y)	Burden (Tg)	AOD
Full size range	2751	22.1	0.020
<10 m	2321	18.2	0.017

associated to dust RF with our model. First, the impact of the choice of the observational size range for constraining the emissions was already estimated as 20% (section 4.2). Second, the uncertainty associated with the magnitude of the dust cycle and the spatial distribution of dust in response to the meteorology is estimated as the coefficient of variation (standard deviation/mean*100) of the net TOA RF from the C4fn, C4wn, and C5wn group of runs, which is 57%. Third we consider the uncertainty related to the size distribution, again calculating the coefficient of variation of the couple C4fn and C4fn-s2 for the net TOA RF (18%). For the LGM we assume the uncertainties for the first two are the same as for the current climate, but we consider the C4fn-lgm, C4fn-lgm-s2 couple for the estimation of the size uncertainty (18%).

The total uncertainty is derived as the root of the quadrature sum of the three elements described, resulting in an overall uncertainty of 63%. If we apply this to the reference estimate with C4fn and C4fn-lgm, this results in a net TOA RF for dust of -0.23 ± 0.14 W/m^2 for the current climate and -0.32 ± 0.20 W/m^2 for the LGM.

These estimates of uncertainty are related just to the "internal" variability of the model used, and do not account for biases/errors related to processes not considered by the model and the parameterizations used. These include uncertainties related to surface albedo and the spatially fixed mineralogical composition of dust, which does not account for varying refractive indices. Some of those additional uncertainties may be accounted for by comparing to other models, although there may also be biases across all models for these estimates.

5. Conclusions

In this work we have refined the dust parameterization set included in CAM4 and CAM5, parts of the CESM model. We restored updated dust optical properties [e.g., *Yoshioka et al*., 2007] based on realistic absorption coefficients [e.g., *Kaufmann et al*., 2001; *Sinyuk et al*., 2003], compared to the obsolete optical properties that were erroneously put in the release versions of CESM. In addition, we refined the CAM4 wet deposition parameterizations [e.g., *Andronache*, 2003] and we updated the soil erodibility maps [*Mahowald et al*., 2006b] in order to give a better representation of the magnitude and spatial distribution of the dust cycle, also accounting for the limited available information of dust provenance at remote sites. Notably, for scaling the soil erodibility maps and for model-observations comparisons we considered observations consistent with the model's size range [e.g., *Cakmur et al*., 2006] and estimated a 20% error if ignoring this constraint. Finally, the most novel change we adopted is a new size distribution for dust emissions, based on *Kok* [2011].

Our results show that the model is able to capture the overall magnitude and spatial variability of dust cycle, but at the same time highlight the difficulty in improving compared to previous work [e.g., *Mahowald et al*., 2006b; *Cakmur et al*., 2006]. As widely recognized, accurately estimating dust emissions in terms of magnitude, timing, and geographical location still remains a major challenge [e.g., *Huneeus et al*., 2011]. A significant improvement over previous work is due to the new size distribution, which shows a good agreement with observations especially for the supermicron size range over a wide range of spatial scales, from the dust sources to remote sites.

For users of the Community Atmosphere Model, we show a methodology that can be used to tune different versions of the model to obtain better matches with observations, following previous work [e.g., *Cakmur et al*., 2006]. An interesting facet of this tuning procedure is that different versions of the model show quite different ability to simulate different parts of the dust cycle (Figures 6–8 and Table 4). The role of resolution is not clear in the literature, as some studies show a small sensitivity of only 20% in emissions and lifetime [e.g., *Mahowald et al*., 2006b], while other studies suggest larger sensitivity [e.g., *Ridley et al*., 2013]. Our results suggest that within one model it is possible to obtain quite different dust cycles, as seen for studies

across multiple models [*Huneeus et al*., 2011]. Notice that differences between online meteorology and reanalyses driven meteorology show very strong changes in the results for the global cycle: we cannot tune the model using reanalysis winds, and then use the same model version with online winds and obtain a good simulation. In most cases, the reanalyses driven meteorology is better (especially for the seasonal cycles), but the online wind driven model has a better simulation of the extent of the North African plume (e.g., Figure 4).

The analysis of the effects that the improved parameterization set developed in this work has on dust RF was analyzed in its components and the uncertainties internal to the model processes were evaluated. The comparison with observational-based estimates of dust RF efficiency shows that our model is able to reproduce these features realistically, both over North Africa [*Zhang and Christopher*, 2003; *Patadia et al*., 2008] and the North Atlantic Ocean [*Li et al*., 2004].

Uncertainties in dust optical properties [*Perlwitz et al*., 2001] also related to the size distribution of dust [*Tegen and Lacis*, 1996; *Sokolik and Toon*, 1996], especially for the smaller but also the upper limits of the model (0.1–10 μm) size distributions [*Reid et al*., 2003], will combine with uncertainties in the magnitude and spatial distribution of dust to render the balance between dust LW and SW interactions very sensitive, causing the wide range of estimates [*Forster et al*., 2007] for dust RF at the TOA.

After considering the uncertainties in our work we calculate a value of -0.23 ± 0.14 W/m^2 as an estimate for the dust global net TOA RF for current climate, and -0.32 ± 0.20 W/m^2 for the LGM climate in our model.

In summary the refined parameterization set developed in this work improves the ability of CAM to represent the global dust cycle, most notably because of much better constraints on the size distributions of dust. Other findings of our study include (1) that the magnitude of the global dust cycle is still highly uncertain, as shown by the result that models with very different global dust emissions and loads compare equally well to the observations—suggesting also that caution should be taken when interpreting those metrics, and (2) a lower dust forcing in the LGM than previous estimates, in part related to smaller emissions, in part to increased atmospheric heating over bright surfaces (deserts and ice) and reduced surface cooling over dark surfaces (oceans).

Acknowledgments
We acknowledge the support of NSF-0932946 and 1003509, 0745961, 1137716, and doeDE-SC00006735. S. Albani acknowledges funding from "Dote ricercatori": FSE, Regione Lombardia. The AERONET data were retrieved online at http://aeronet.gsfc.nasa.gov. We thank the Principal Investigators and their staff for establishing and maintaining the sites used in this work. We gratefully acknowledge Joseph Prospero for providing dust surface concentration data from in situ measurements from the University of Miami Ocean Aerosol Network. We appreciated the constructive comments from Ron Miller and from two anonymous reviewers that helped improving our manuscript. These simulations were conducted at the National Center for Atmospheric Research's Computation Information Systems Laboratory, an NSF funded facility.

References

Albani, S., B. Delmonte, V. Maggi, C. Baroni, J. R. Petit, B. Stenni, C. Mazzola, and M. Frezzotti (2012a), Interpreting last glacial to Holocene dust changes at Talos Dome (East Antarctica): Implications for atmospheric variations from regional to hemispheric scales, *Clim. Past*, *8*, 741–750, doi:10.5194/cp-8-741-2012.

Albani, S., N. M. Mahowald, B. Delmonte, V. Maggi, and G. Winckler (2012b), Comparing modeled and observed changes in mineral dust transport and deposition to Antarctica between the Last Glacial Maximum and current climates, *Clim. Dyn.*, *38*(9), 1731–1755, doi:10.1007/s00382-011-1139-5.

Alfaro, S. C., and L. Gomes (2001), Modeling mineral aerosol production by wind erosion: Emission intensities and aerosol size distributions in source areas, *J. Geophys. Res.*, *106*(D16), 18,075–18,084.

Andronache, C. (2003), Estimated variability of below-cloud aerosol removal by rainfall for observed aerosol size distributions, *Atmos. Chem. Phys.*, *3*, 131–143.

Balkanski, Y., M. Schultz, T. Claquin, and S. Guibert (2007), Reevaluation of mineral aerosol radiative forcings suggests a better agreement with satellite and AERONET data, *Atmos. Chem. Phys.*, *7*, 81–95.

Balkanski, Y. J., D. J. Jacob, G. M. Gardner, W. C. Graustein, and K. K. Turekian (1993), Transport and residence times of tropospheric aerosols inferred from a global three-dimensional simulation of 210Pb, *J. Geophys. Res.*, *98*(D11), 20,573–20,586.

Bonan, G. B., S. Levis, L. Kergoat, and K. W. Oleson (2002), Landscapes as patches of plant functional types: An integrating concept for climate and ecosystem models, *Global Biogeochem. Cycles*, *16*(2), 1021, doi:10.1029/2000GB001360.

Brady, E. C., B. L. Otto-Bliesner, J. E. Kay, and N. Rosenbloom (2013), Sensitivity to glacial forcing in the CCSM4, *J. Clim.*, *26*, 1901–1925, doi:10.1175/JCLI-D-11–00416.1.

Cakmur, R. V., R. L. Miller, J. Perlwitz, I. V. Geogdzhayev, P. Ginoux, D. Koch, K. E. Kohfeld, I. Tegen, and C. S. Zender (2006), Constraining the magnitude of the global dust cycle by minimizing the difference between a model and observations, *J. Geophys. Res.*, *111*, D06207, doi:10.1029/2005JD005791.

Chylek, P., and U. Lohmann (2008), Aerosol radiative forcing and climate sensitivity deduced from the Last Glacial Maximum to Holocene transition, *Geophys. Res. Lett.*, *35*, L04804, doi:10.1029/2007GL032759.

Claquin, T., M. Schulz, and Y. J. Balkanski (1999), Modeling the mineralogy of atmospheric dust sources, *J. Geophys. Res.*, *104*(D18), 22,243–22,256, doi:10.1029/1999JD900416.

Claquin, T., et al. (2003), Radiative forcing of climate by ice-age atmospheric dust, *Clim. Dyn.*, *20*, 193–202.

Colarco, P. R., O. B. Toon, O. Torres, and P. J. Rasch (2002), Determining the UV imaginary index of refraction of Saharan dust particles from Total Ozone Monitoring data using a three-dimensional model of dust transport, *J. Geophys. Res.*, *107*(D16), 4289, doi:10.1029/2001JD000903.

Conway, H., A. Gades, and C. F. Raymond (1996), Albedo of dirty snow during conditions of meltwater, *Water Res. Res.*, *32*(6), 1713–1718.

d'Almeida, G. A. (1997), On the variability of desert aerosol radiative characteristics, *J. Geophys. Res.*, *92*(D3), 3017–3026.
d'Almeida, G. A., P. Koepke, and P. E. Shettle (1991), Atmospheric Aerosols: Global Climatology and Radiative Characteristics, 561 pp., A. Deepak. Publ, Hampton, Va.
Dana, M. T., and J. M. Hales (1976), Statistical aspects of the washout of polydisperse aerosols, *Atmos. Environ.*, *10*, 44–50.
Delmonte, B., J.-R. Petit, K. K. Andersen, I. Basile-Doelsch, V. Maggi, and V. Y. Lipenkov (2004), Dust size evidence for opposite regional atmospheric circulation changes over east Antarctica during the last climatic transition, *Clim. Dyn.*, *23*, 427–438, doi:10.1007/s00382-004-0450-9.
deMenocal, P., J. Ortiz, T. Guilderson, J. Adkins, M. Sarnthein, L. Baker, and M. Yarusinsky (2000), Abrupt onset and termination of the African Humid Period: Rapid climate responses to gradual insolation forcing, *Quat. Sci. Rev.*, *19*(1–5), 347–361.
Dubovik, O., and M. D. King (2000), A flexible inversion algorithm for retrieval of aerosol optical properties from Sun and sky radiance measurements, *J. Geophys. Res.*, *105*(D16), 20,673–20,696.
Dubovik, O., B. Holben, T. F. Eck, A. Smirnov, Y. J. Kaufman, M. D. King, D. Tanré, and I. Slutsker (2002), Variability of absorption and optical properties of key aerosol types observed in worldwide locations, *J. Atmos. Sci.*, *69*, 590–608.
Dubovik, O. et al. (2006), Application of spheroid models to account for aerosol particle nonsphericity in remote sensing of desert dust, *J. Geophys. Res.*, *111*(D11), D11208, doi:10.1029/2005JD006619.
Fécan, F., B. Marticorena, and G. Bergametti (1999), Parametrization of the increase of the aeolian erosion threshold wind friction velocity due to soil moisture for arid and semi-arid areas, *Ann. Geophys.*, *17*, 149–157.
Flanner, M. G., C. S. Zender, J. T. Randerson, and P. J. Rasch (2007), Present-day climate forcing and response from black carbon in snow, *J. Geophys. Res.*, *112*, D11202, doi:10.1029/2006JD008003.
Formenti, P., et al. (2011), Recent progress in understanding physical and chemical properties of African and Asian mineral dust, *Atmos. Chem. Phys.*, *11*, 8231–8256.
Forster, P., et al. (2007), Changes in atmospheric constituents and in radiative forcing, in Climate Change 2007: The Physical Science Basis, Contribution of Working Group I to the Fourth Assessment Report of the Intergovernmental Panel on Climate Change, edited by S. Solomon et al., pp. 130–234, Cambridge Univ. Press, Cambridge, U. K.
Gent, P. R., et al. (2011), The community climate system model, version 4, *J. Clim.*, *24*(19), 4973–4991.
Ghan, S. J., and R. A. Zaveri (2007), Parameterization of optical properties for hydrated internally mixed aerosol, *J. Geophys. Res.*, *112*, D10201, doi:10.1029/2006JD007927.
Ghan, S. J., X. Liu, R. C. Easter, R. Zaveri, P. J. Rasch, and J.-H. Yoon (2012), Toward a minimal representation of aerosols in climate models: Comparative decomposition of aerosol direct, semidirect, and indirect radiative forcing, *J. Clim.*, *25*, 6461–6476.
Gillette, D. A., B. Marticorena, and G. Bergametti (1998), Change in the aerodynamic roughness height by saltating grains: Experimental assessment, test of theory, and operational parameterization, *J. Geophys. Res.*, *103*(D6), 6203–6209.
Ginoux, P., M. Chin, I. Tegen, J. Prospero, B. Holben, O. Dubovik, and S.-J. Lin (2001), Sources and distributions of dust aerosols simulated with the GOCART model, *J. Geophys. Res.*, *106*(D17), 20,255–20,273.
Han, Q., and C. S. Zender (2010), Desert dust aerosol age characterized by mass-age tracking of tracers, *J. Geophys. Res.*, *115*, D22201, doi:10.1029/2010JD014155.
Heintzenberg, J. (2009), The SAMUM-1 experiment over Southern Morocco: Overview and introduction, *Tellus, Ser. B*, *61*, 2–11.
Hess, M., P. Koepke, and I. Schult (1998), Optical properties of aerosols and clouds: The software package OPAC, *Bull. Am. Meteorol. Soc.*, *79*, 831–844.
Holben, B. N., et al. (1998), AERONET—A federated instrument network and data archive for aerosol characterization, *Remote Sens. Environ.*, *66*, 1–16.
Huneeus, N., et al. (2011), Global dust model intercomparison in Aerocom phase I, *Atmos. Chem. Phys.*, *11*, 7781–7816.
Iversen, J. D., and B. R. White (1982), Saltation threshold on Earth, Mars, and Venus, *Sedimentology*, *29*, 111–119.
Jacobson, M. Z. (2001), Global direct radiative forcing due to multicomponent anthropogenic and natural aerosols, *J. Geophys. Res.*, *106*(D2), 1551–1568.
Kaplan, J. O., et al. (2003), Climate change and Arctic ecosystems: 2. Modeling, paleodata-model comparisons, and future projections, *J. Geophys. Res.*, *108*(D19), 8171, doi:10.1029/2002JD002559.
Kaufmann, Y. J., D. Tanré, O. Dubovik, A. Karnieli, and L. A. Remer (2001), Absorption of sunlight by dust as inferred from satellite and ground-based remote sensing, *Geophys. Res. Lett.*, *28*(8), 1479–1482.
Koffi, B., et al. (2012), Application of the CALIOP layer product to evaluate the vertical distribution of aerosols estimated by global models: Aerocom phase I results, *J. Geophys. Res.*, *117*, D10201, doi:10.1029/2011JD016858.
Kohfeld, K. E., and S. P. Harrison (2001), DIRTMAP: The geological record of dust, *Earth Sci. Rev.*, *54*, 81–114.
Köhler, P., R. Bintanja, H. Fischer, F. Joos, R. Knutti, G. Lohmann, and V. Masson-Delmotte (2010), What caused Earth's temperature variations during the last 800,000 years? Data-based evidence on radiative forcing and constraints on climate sensitivity, *Quat. Sci. Rev.*, *29*(1–2), 129–145.
Kok, J. F. (2011), A scaling theory for the size distribution of emitted dust aerosols suggests climate models underestimate the size of the global dust cycle, *Proc. Natl. Acad. Sci. U. S. A.*, *108*, 1016–1021, doi:10.1073/pnas.1014798108.
Lafon, S., I. N. Sokolik, J. L. Rajot, S. Caquineau, and A. Gaudichet (2006), Characterization of iron oxides in mineral dust aerosols: Implications for light absorption, *J. Geophys. Res.*, *111*, D21207, doi:10.1029/2005JD007016.
Lamarque, J.-F., et al. (2010), Historical (1850–2000) gridded anthropogenic and biomass burning emissions of reactive gases and aerosols: Methodology and application, *Atmos. Chem. Phys.*, *10*, 7017–7039.
Lambert, F., B. Delmonte, J.-R. Petit, M. Bigler, P. R. Kaufmann, M. A. Hutterli, T. F. Stocker, U. Ruth, J. P. Steffensen, and V. Maggi (2008), Dust-climate couplings over the past 800,000 years from the EPICA Dome C ice core, *Nature*, *452*, 616–619, doi:10.1038/nature06763.
Lawrence, C. R., and J. C. Neff (2009), The contemporary physical and chemical flux of Aeolian dust: A synthesis of direct measurements of dust deposition, *Chem. Geol.*, *257*, 46–63.
Lawrence, D. M., et al. (2011), Parameterization improvements and functional and structural advances in version 4 of the Community Land Model, *J. Adv. Model. Earth Syst.*, *3*, M03001, doi:10.1029/2011MS000045.
Lawrence, P. J., and T. N. Chase (2007), Representing a MODIS consistent land surface in the Community Land Model (CLM 3.0), *J. Geophys. Res.*, *112*, G01023, doi:10.1029/2006JG000168.
Li, F., A. M. Vogelmann, and V. Ramanathan (2004), Saharan dust aerosol radiative forcing measured from space, *J. Clim.*, *17*, 2558–2571.
Liao, H., J. H. Seinfeld, P. J. Adams, and L. J. Mickley (2004), Global radiative forcing of coupled tropospheric ozone and aerosols in a unified general circulation model, *J. Geophys. Res.*, *109*, D16207, doi:10.1029/2003JD004456.

Liu, X., et al. (2012), Toward a minimal representation of aerosols in climate models: Description and evaluation in the Community Atmosphere Model CAM5, *Geosci. Model Dev.*, *5*, 709–739, doi:10.5194/gmd-5–709-2012.
Lunt, D. J., and P. J. Valdes (2002), Dust deposition and provenance at the Last Glacial Maximum and present day, *Geophys. Res. Lett.*, *29*(22), 2085, doi:10.1029/2002GL015656.
Maher, B. A., J. M. Prospero, D. Mackie, D. Gaiero, P. P. Hesse, and Y. Balkanski (2010), Global connections between aeolian dust, climate and ocean biogeochemistry at the present day and at the last glacial maximum, *Earth Sci. Rev.*, *99*, 61–97.
Mahowald, N. (2011), Aerosol indirect effects on biogeochemistry and climate, *Science*, *334*, 794, doi:10.1126/science.1207374.
Mahowald, N., K. Kohfeld, M. Hansson, Y. Balkanski, S. P. Harrison, I. C. Prentice, M. Schulz, and H. Rodhe (1999), Dust sources and deposition during the last glacial maximum and current climate: A comparison of model results with paleodata from ice cores and marine sediments, *J. Geophys. Res.*, *104*(D13), 15,895–15,916.
Mahowald, N., S. Albani, S. Engelstaedter, G. Winckler, and M. Goman (2011), Model insight into glacial-interglacial paleodust records, *Quat. Sci. Rev.*, *30*(7–8), 832–854.
Mahowald, N., S. Albani, J. F. Kok, S. Engelstader, R. S. Scanza, D. S. Ward, and M. G. Flanner (2013), The size distribution of desert dust aerosols and its impact on the Earth system, *Aeolian Res.*, doi:10.1016/j.aeolia.2013.09.002.
Mahowald, N. M., J.-F. Lamarque, X. Tie, and E. Wolff (2006a), Sea salt aerosol response to climate change: Last glacial maximum, preindustrial and doubled carbon dioxide climates, *J. Geophys. Res.*, *111*, D05303, doi:10.1029/2005JD006459.
Mahowald, N. M., D. R. Muhs, S. Levis, P. J. Rasch, M. Yoshioka, C. S. Zender, and C. Luo (2006b), Change in atmospheric mineral aerosols in response to climate: Last glacial period, preindustrial, modern, and doubled carbon dioxide climates, *J. Geophys. Res.*, *111*, D10202, doi:10.1029/2005JD006653.
Mahowald, N. M., M. Yoshioka, W. Collins, A. Conley, D. Fillmore, and D. Coleman (2006c), Climate response and radiative forcing from mineral aerosols during the glacial maximum, pre-industrial, current and doubled-carbon dioxide climates, *Geophys. Res. Lett.*, *33*, L20705, doi:10.1029/2006GL026126.
Mahowald, N. M., et al. (2009), Atmospheric iron deposition: Global distribution, variability, and human perturbations, *Annu. Rev. Mar. Sci.*, *1*, 245–278.
Mahowald, N. M., et al. (2010), Observed 20th century desert dust variability: Impact on climate and biogeochemistry, *Atmos. Chem. Phys.*, *10*(22), 10,875–10,893.
Maring, H., D. L. Savoie, M. A. Izaguirre, and L. Custals (2003), Mineral dust aerosols size distribution change during atmospheric transport, *J. Geophys. Res.*, *108*(D19), 8592, doi:10.1029/2002JD002536.
Marticorena, B., and G. Bergametti (1995), Modeling the atmospheric dust cycle: 1. Design of a soil-derived dust emission scheme, *J. Geophys. Res.*, *100*(D8), 16,415–16,430.
Martin, J. H., R. M. Gordon, and S. E. Fitzwater (1990), Iron in Antarctic waters, *Nature*, *353*(6340), 156–158.
McConnell, J. R., A. J. Aristarain, J. R. Banta, P. R. Edwards, and J. C. Simoes (2007), 20th-Century doubling in dust archived in an Antarctic Peninsula ice core parallels climate change and desertification in South America, *Proc. Natl. Acad. Sci. U. S. A.*, *104*(14), 5743–5748.
Miller, R. L., J. P. Perlwitz, and I. Tegen (2004), Feedback upon dust emission by dust radiative forcing through the planetary boundary layer, *J. Geophys. Res.*, *109*, D24209, doi:10.1029/2004JD004912.
Miller, R. L., and I. Tegen (1998), Climate Response to Soil Dust Aerosols, *J. Clim.*, *11*(12), 3247–3267, doi:10.1175/1520-0442(1998)011<3247:CRTSDA>2.0.CO;2.
Miller, R. L., et al. (2006), Mineral dust aerosols in the NASA Goddard Institute for Space Sciences ModelE atmospheric general circulation model, *J. Geophys. Res.*, *111*, D06208, doi:10.1029/2005JD005796.
Mulitza, S., et al. (2010), Increase in African dust flux at the onset of commercial agriculture in the Sahel region, *Nature*, *466*, 226–228, doi:10.1038/nature09213.
Müller, D., et al. (2012), Comparison of optical and microphysical properties of pure Saharan mineral dust observed with AERONET Sun photometer, Raman lidar, and in situ instruments during SAMUM 2006, *J. Geophys. Res.*, *117*, D07211, doi:10.1029/2011JD016825.
Myhre, G., and F. Stordal (2001), Global sensitivity experiments of the radiative forcing due to mineral aerosols, *J. Geophys. Res.*, *106*(D16), 18,193–18,204.
Neale, R. B., et al. (2010a), *Description of the NCAR Community Atmosphere Model (CAM 5.0)*, NCAR Tech. Note, *TN-486*, pp. 268, Natl. Cent. for Atmos. Res., Boulder, Colo.
Neale, R. B., et al. (2010b), *Description of the NCAR Community Atmosphere Model (CAM 4.0)*, NCAR Tech. Note, *TN-485*, pp. 212, Natl. Cent. for Atmos. Res., Boulder, Colo.
Okin, G. S. (2008), A new model of wind erosion in the presence of vegetation, *J. Geophys. Res.*, *113*, F02S10, doi:10.1029/2007JF000758.
Oleson, K. W., et al. (2010), *Technical description of version 4.0 of the Community Land Model (CLM)*, NCAR Tech. Note, *TN-478+STR*, pp. 266, Natl. Cent. for Atmos. Res., Boulder, Colo.
Otto-Bliesner, B. L., S. Joussaume, S. P. Harrison, A. Abe-Ouchi, and P. Braconnot (2009), Modeling and data syntheses of past climates, *Eos Trans. AGU*, *90*(11), 93.
Overpeck, J., D. Rind, A. Lacis, and R. Healy (1996), Possible role of dust-induced regional warming in abrupt climate change during the last glacial period, *Nature*, *384*, 447–449.
Patadia, F., E.-S. Yang, and S. A. Christopher (2008), Does dust change the clear sky top of the atmosphere shortwave flux over high surface reflectance regions?, *Geophys. Res. Lett.*, *36*, L15825, doi:10.1029/2009GL039092.
Patterson, E. M., D. A. Gillette, and B. H. Stockton (1977), Complex index of refraction between 300 and 700 nm of Saharan dust aerosols, *J. Geophys. Res.*, *82*(21), 16,595–16,969.
Perlwitz, J., and R. L. Miller (2010), Cloud cover increase with increasing aerosol absorptivity: A counterexample to the conventional semidirect aerosol effect, *J. Geophys. Res.*, *115*, D08203, doi:10.1029/2009JD012637.
Perlwitz, J., I. Tegen, and R. L. Miller (2001), Interactive soil dust aerosol model in the GISS GCM 1: Sensitivity of the soil dust cycle to radiative properties of soil dust aerosols, *J. Geophys. Res.*, *106*(D16), 18,167–18,192, doi:10.1029/2000JD900668.
Petit, J.-R., et al. (1999), Climate and atmospheric history of the past 420,000 years from the Vostok ice core, Antarctica, *Nature*, *399*, 429–436.
Prospero, J. M., and P. J. Lamb (2003), African droughts and dust transport to the Caribbean: Climate change implications, *Science*, *302*(5647), 1024–1027, doi:10.1126/science.1089915.
Prospero, J. M., and R. T. Nees (1986), Impact of the North African drought and El Niño on mineral dust in the Barbados trade winds, *Nature*, *320*, 735–738.
Prospero, J. M., M. Uematsu, and D. L. Savoie (1989), Mineral aerosol transport to the Pacific Ocean, in Chemical Oceanography, vol. *10*, edited by J. P. Riley, R. Chester, and R. A. Duce, pp. 188–218, Academic, San Diego, Calif.

Prospero, J. M., P. Ginoux, O. Torres, S. E. Nicholson, and T. E. Gill (2002), Environmental characterization of global sources of atmospheric soil dust identified with the Nimbus 7 Total Ozone Mapping Spectrometer (TOMS) Absorbing Aerosol Product, *Rev. Geophys.*, *40*(1), 1002, doi:10.1029/2000RG000095.

Pye, K. (1987), *Aeolian Dust and Dust Deposits*, pp. 334, Academic, London.

Pye, K. (1995), The origin, nature and accumulation of loess, *Quat. Sci. Rev.*, *14*(7–8), 653–667.

Rea, D. K. (1994), The paleoclimatic record provided by eolian deposition in the deep sea: The geologic history of wind, *Rev. Geophys.*, *32*(2), 159–195.

Reddy, M. S., O. Boucher, Y. Balanski, and M. Schulz (2005), Aerosol optical depths and direct radiative perturbations by species and source type, *Geophys. Res. Lett.*, *32*, L12803, doi:10.1029/2004GL021743.

Reid, J. S., et al. (2003), Comparison of size and morphological measurements of coarse mode dust particles from Africa, *J. Geophys. Res.*, *108*(D19), 8593, doi:10.1029/2002JD002485.

Ridley, D., C. Heald, J. Pierce, and M. J. Evans (2013), Toward resolution-independent dust emissions in global models: Impacts on the seasonal and spatial distribution of dust, *Geophys. Res. Lett.*, *40*, 3873–2877, doi:10.1002/grl.50409.

Ryder, C. L., et al. (2013), Optical properties of Saharan dust aerosol and contribution from the coarse mode as measured during the Fennec 2011 aircraft campaign, *Atmos. Chem. Phys.*, *13*, 303–325.

Schulz, M., Y. J. Balkanski, W. Guelle, and F. Dulac (1998), Role of aerosol size distribution and source location in a three-dimensional simulation of a Saharan dust episode tested against satellite-derived optical thickness, *J. Geophys. Res.*, *103*(D9), 10,579–10,592, doi:10.1029/97JD02779.

Shao, Y., K.-H. Wyrwoll, A. Chappell, J. Huang, Z. Lin, G. H. McTainsh, M. Mikami, T. Y. Tanaka, X. Wang, and S. Yoon (2011), Dust cycle: An emerging core theme in Earth system science, *Aeol. Res.*, *2*, 181–204.

Sinyuk, A., O. Torres, and O. Dubovik (2003), Combined use of satellite and surface observations to infer the imaginary part of refractive index of Saharan dust, *Geophys. Res. Lett.*, *30*(2), 1081, doi:10.1029/2002GL016189.

Sokolik, I. N., and O. B. Toon (1996), Direct radiative forcing by anthropogenic airborne mineral aerosols, *Nature*, *381*, 681–683.

Sokolik, I. N., and O. B. Toon (1999), Incorporation of mineralogical composition into models of the radiative properties of mineral aerosol from UV to IR wavelengths, *J. Geophys. Res.*, *104*(D8), 9423–9444, doi:10.1029/1998JD200048.

Sokolik, I. N., O. B. Toon, and R. W. Bergstrom (1998), Modeling the radiative characteristics of airborne mineral aerosols at infrared wavelengths, *J. Geophys. Res.*, *103*(D8), 8813–8826, doi:10.1029/98JD00049.

Steffensen, J. P. (1997), The size distribution of microparticles from selected segments of the Greenland Ice Core Project ice core representing different climatic periods, *J. Geophys. Res.*, *102*(C12), 26,755–26,763.

Stuut, J. B., M. Zabel, V. Ratmeier, P. Helmke, E. Schefuss, G. Lavik, and R. Schneide (2005), Provenance of present day eolian dust collected off NW Africa, *J. Geophys. Res.*, *110*(D4), D04202, doi:10.1029/2004JD005161.

Takemura, T., M. Egashira, K. Matsuzawa, H. Ichijo, R. O'ishi, and A. Abe-Ouchi (2009), A simulation of the global distribution and radiative forcing of soil dust aerosols at the Last Glacial Maximum, *Atmos. Chem. Phys.*, *9*, 3061–3073.

Tanré, D., Y. J. Kaufman, B. N. Holben, B. Chatenet, A. Karnieli, F. Lavenu, L. Blarel, O. Dubovik, L. A. Remer, and A. Smirnov (2001), Climatology of dust aerosol size distribution and optical properties derived from remotely sensed data in the solar spectrum, *J. Geophys. Res.*, *106*(D16), 18205, doi:10.1029/2000JD900663.

Taylor, K. E. (2001), Summarizing multiple aspects of model performance in a single diagram, *J. Geophys. Res.*, *106*(D7), 7183–7192.

Taylor, K. E., R. J. Stouffer, and G. A. Meehl (2012), An overview of CMIP5 and the experiment design, *Bull. Am. Meteorol. Soc.*, *93*, 485–498, doi:10.1175/BAMS-D-11-00094.1.

Tegen, I. (2003), Modeling the mineral dust aerosol cycle in the climate system, *Quat. Sci. Rev.*, *22*, 1821–1834.

Tegen, I., and I. Fung (1994), Modeling of mineral dust in the atmosphere—Sources, transport, and optical thickness, *J. Geophys. Res.*, *99*(D11), 22,897–22,914.

Tegen, I., and A. A. Lacis (1996), Modeling of particle size distribution and its influence on the radiative properties of mineral dust aerosol, *J. Geophys. Res.*, *101*(D14), 19,237–19,244.

Tegen, I., S. P. Harrison, K. Kohfeld, I. C. Prentice, M. Coe, and M. Heimann (2002), Impact of vegetation and preferential source areas on global dust aerosol: Results from a model study, *J. Geophys. Res.*, *107*(D21), 4576, doi:10.1029/2001JD000963.

Videen, G., and P. Chýlek (1998), Scattering by a composite sphere with an absorbing inclusion and effective medium approximations, *Opt. Commun.*, *158*, 1–6.

Volz, F. E. (1973), Infrared optical constants of ammonium sulfate, Sahara dust, volcanic pumice, and flyash, *Appl. Opt.*, *12*, 564–568.

Werner, M., I. Tegen, S. P. Harrison, K. E. Kohfeld, I. C. Prentice, Y. Balkanski, H. Rodhe, and C. Roelandt (2002), Seasonal and interannual variability of the mineral dust cycle under present and glacial climate conditions, *J. Geophys. Res.*, *107*(D24), 4744, doi:10.1029/2002JD002365.

White, B. R. (1979), Soil transport by winds on Mars, *J. Geophys. Res.*, *84*(B9), 4643–4651.

Wild, M. (2008), Short-wave and long-wave surface radiation budgets in GCMs: A review based on the IPCC-AR4/CMIP3 models, *Tellus, Ser. A*, *60*, 932–945.

Wu, G., T. Yao, B. Xu, L. Tian, C. Zhang, and X. Zhang (2009), Volume-size distribution of microparticles in ice cores from the Tibetan Plateau, *J. Glaciol.*, *55*(193), 859–868.

Yoshioka, M., N. Mahowald, A. Conley, W. Collins, D. Fillmore, C. Zender, and D. Coleman (2007), Impact of desert dust radiative forcing on Sahel precipitation: Relative importance of dust compared to sea surface temperature variations, vegetation changes and greenhouse gas warming, *J. Clim.*, *20*, 1445–1467, doi:10.1175/JCLI4056.1.

Zender, C. S., H. Bian, and D. Newman (2003a), Mineral dust entrainment and deposition (DEAD) model: Description and 1990s dust climatology, *J. Geophys. Res.*, *108*(D14), 4416, doi:10.1029/2002JD002775.

Zender, C. S., D. Newman, and O. Torres (2003b), Spatial heterogeneity in aeolian erodibility: Uniform, topographic, geomorphic, and hydrologic hypotheses, *J. Geophys. Res.*, *108*(D17), 4543, doi:10.1029/2002JD003039.

Zhang, J., and S. A. Christopher (2003), Longwave radiative forcing of Saharan dust aerosols estimated from MODIS, MISR, and CERES observations on Terra, *Geophys. Res. Lett.*, *30*(23), 2188, doi:10.1029/2003GL018479.